

The inverse Kalman filter

Xinyi Fang and Mengyang Gu*

Abstract

In this study, we introduce a new approach, the inverse Kalman filter (IKF), which enables accurate matrix-vector multiplication between a covariance matrix from a dynamic linear model and any real-valued vector with linear computational cost. We incorporate the IKF with the conjugate gradient algorithm, which substantially accelerates the computation of matrix inversion for a general form of covariance matrices, whereas other approximation approaches may not be directly applicable. We demonstrate the scalability and efficiency of the IKF approach through distinct applications, including nonparametric estimation of particle interaction functions and predicting incomplete lattices of correlated data, using both simulation and real-world observations, including cell trajectory and satellite radar interferogram.

1 Introduction

Dynamic linear models (DLMs) or linear state space models are ubiquitously used in modeling temporally correlated data [54, 8]. Each observation $y_t \in \mathbb{R}$ in DLMs is associated with a q -dimensional latent state vector $\boldsymbol{\theta}_t$, defined as:

$$y_t = \mathbf{F}_t \boldsymbol{\theta}_t + v_t, \quad v_t \sim \mathcal{N}(0, V_t), \quad (1)$$

$$\boldsymbol{\theta}_t = \mathbf{G}_t \boldsymbol{\theta}_{t-1} + \mathbf{w}_t, \quad \mathbf{w}_t \sim \mathcal{MN}(\mathbf{0}, \mathbf{W}_t), \quad (2)$$

where \mathbf{F}_t and \mathbf{G}_t are matrices of dimensions $1 \times q$ and $q \times q$, respectively, \mathbf{W}_t is a $q \times q$ covariance matrix for $t = 2, \dots, N$, and the initial state vector $\boldsymbol{\theta}_1 \sim \mathcal{MN}(\mathbf{b}_1, \mathbf{W}_1)$ with $\mathbf{b}_1 = \mathbf{0}$ assumed in our application. The dependent structure of DLMs is illustrated in Fig. 1(a), where each observation y_t is associated with a single latent state $\boldsymbol{\theta}_t$, with the mean of the observation being $z_t = \mathbf{F}_t \boldsymbol{\theta}_t$.

DLMs are a flexible class of models that include many widely used processes, such as autoregressive and moving average processes [37, 40]. Some Gaussian processes (GPs) with commonly used kernel functions, such as the Matérn covariance with a half-integer roughness parameter [20], can also be represented as DLMs [55, 21], with closed-form expressions for \mathbf{F}_t , \mathbf{G}_t and \mathbf{W}_t . This connection, summarized in the Supplementary Material, enables the construction of differentiable processes within the DLM framework, resulting in more efficient models for estimating smooth functions from noisy observations.

The Kalman filter (KF) provides a scalable approach for estimating latent state and computing likelihood in DLMs, which scales linearly with the number of observations [24], as reviewed in Appendix A. In particular, the KF enables efficient computation of $\mathbf{L}^{-1} \mathbf{u}$ for any N -dimensional vector \mathbf{u} in $\mathcal{O}(q^3 N)$ operations, where \mathbf{L} is the Cholesky factor of the covariance matrix $\boldsymbol{\Sigma} = \text{cov}[\mathbf{y}_{1:N}] = \mathbf{L} \mathbf{L}^T$ (See Lemma 6 in the Appendix).

*The authors contribute equally. Correspondence should be addressed to Mengyang Gu (mengyang@pstat.ucsb.edu)

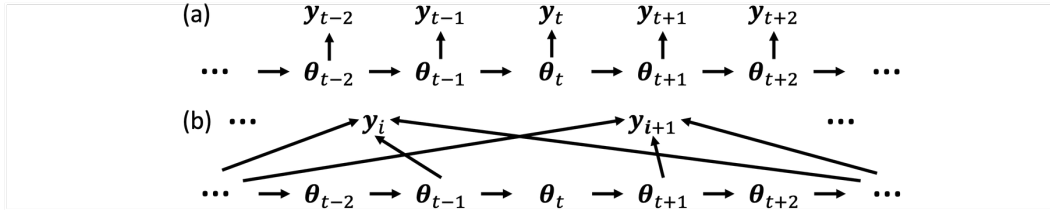


Figure 1: The dependent structure of the dynamic linear model (panel (a)) and particle dynamics (panel (b)).

Computational challenges remain for high-dimensional state space models and scenarios where KF cannot be directly applied, such as the dependent structure shown in Fig. 1(b), where each observation y_i can be associated with multiple latent states. This interaction structure is common in fundamental simulation models in physics, such as the molecular dynamics simulation [41]. Details of modeling interactions are introduced in Section 3. One way to overcome these challenges is to efficiently compute $\Sigma \mathbf{u}$ for any N -dimensional vector \mathbf{u} and utilize the optimization methods such as the conjugate gradient (CG) algorithm for computing the predictive distribution [23, 19]. This strategy has been used to approximate the maximum likelihood estimator of parameters in GPs [47, 35]. Yet, each CG iteration requires matrix-vector multiplication, which involves $\mathcal{O}(N^2)$ operations and storage, making it prohibitive for large N .

To address this issue, we propose a new algorithm, the *Inverse Kalman filter*, which computes $\mathbf{L}\mathbf{u}$ and $\mathbf{L}^T\mathbf{u}$ for any N -dimensional vector \mathbf{u} with $\mathcal{O}(q^3N)$ operations without approximations. By integrating IKF with the CG algorithm, our approach offers a scalable way for problems with a general covariance structure of the observations, $\sum_{j=1}^J \mathbf{A}_j \Sigma_j \mathbf{A}_j^T + \Lambda$, where Σ_j is a covariance matrix induced by a DLM, \mathbf{A}_j is a sparse matrix, and Λ is a diagonal matrix. This structure is common in statistical models such as latent factor models, varying coefficient models [22], and autoregressive models with exogenous inputs [31]. Our approach is motivated by nonparametric estimation of particle interaction functions [32] by a large number of particles over a long time, whereas approximation methods may not be directly applicable. We also demonstrate its accuracy in predicting missing values in the incomplete lattice of correlated data [46], and compare with various approximation methods [51, 27, 5, 11, 15, 14]. We introduce these applications in Section 3, with results presented in Sections 4 - 5.

The primary contribution of this article is the development of the Inverse Kalman filter, which reduces the computational and storage cost of matrix-vector multiplication $\Sigma \mathbf{u}$ from $\mathcal{O}(N^2)$ to $\mathcal{O}(q^3N)$. This is generally applicable to any $N \times N$ covariance Σ induced by DLMS, where q is a small number of latent states, not larger than 3 in our applications. Additionally, we integrate the IKF technique into a CG algorithm for computing the predictive distribution in GPs, thereby reducing the computational complexity by a few orders of magnitude with almost no approximation in our applications. Parameter estimation is achieved via either cross-validation or maximum likelihood estimation, both of which are substantially accelerated with the proposed approach.

2 Inverse Kalman filter

In this section, we introduce an exact algorithm for computing $\Sigma \mathbf{u}$ with $\mathcal{O}(q^3N)$, where \mathbf{u} is an N -dimensional real-valued vector and $\Sigma = \text{cov}[\mathbf{y}_{1:N}]$ is an $N \times N$ covariance matrix of the observations induced by a DLM with q latent states in Eq. (1). Denote $\Sigma = \mathbf{L}\mathbf{L}^T$, where the Cholesky factor \mathbf{L} does not need to be explicitly computed in our approach. We provide fast

Algorithm 1 Inverse Kalman filter (IKF) for computing $\Sigma \mathbf{u}$.

Input: $\mathbf{F}_t, \mathbf{G}_t, \mathbf{W}_t, t = 1, \dots, N$, an N -dimensional vector \mathbf{u} .

- 1: Use Kalman filter from Lemma 5 to compute \mathbf{B}_t, Q_t , and \mathbf{K}_t for $t = 1, \dots, N$.
- 2: Use Lemma 1 to compute $\tilde{\mathbf{x}} = \mathbf{L}^T \mathbf{u}$.
- 3: Use Lemma 2 to compute $\mathbf{x} = \mathbf{L} \tilde{\mathbf{x}}$.

Output: \mathbf{x} .

algorithms to compute $\tilde{\mathbf{x}} = \mathbf{L}^T \mathbf{u}$ and $\mathbf{x} = \mathbf{L} \tilde{\mathbf{x}}$ by Lemma 1 and Lemma 2, respectively, each with $\mathcal{O}(q^3 N)$ operations. Detailed proofs of these lemmas are available in Appendix B. In the following, u_t, x_t, \tilde{x}_t denote the t th elements of the vector of \mathbf{u}, \mathbf{x} , and $\tilde{\mathbf{x}}$, respectively, for $t = 1, 2, \dots, N$. Additionally, $L_{t',t}$ denotes the (t', t) th element of \mathbf{L} .

Lemma 1 (Compute $\tilde{\mathbf{x}} = \mathbf{L}^T \mathbf{u}$ with linear computational cost). *For any N -vector \mathbf{u} , let $\tilde{x}_N = Q_N^{1/2} u_N$, $\mathbf{g}_{N-1} = \mathbf{F}_N \mathbf{G}_N u_N$, and $\tilde{x}_{N-1} = Q_{N-1}^{1/2} (\ell_{N,N-1} u_N + u_{N-1})$. For $t = N-2, \dots, 1$, iteratively compute \tilde{x}_t by*

$$\tilde{x}_t = Q_t^{\frac{1}{2}} \left(\tilde{\ell}_{t+1,t} + \ell_{t+1,t} u_{t+1} + u_t \right), \quad (3)$$

$$\mathbf{g}_t = \mathbf{g}_{t+1} \mathbf{G}_{t+1} + \mathbf{F}_{t+1} \mathbf{G}_{t+1} u_{t+1}, \quad (4)$$

where $\ell_{t+1,t} = \mathbf{F}_{t+1} \mathbf{G}_{t+1} \mathbf{K}_t$, $\tilde{\ell}_{t+1,t} = \mathbf{g}_{t+1} \mathbf{G}_{t+1} \mathbf{K}_t$, and \mathbf{K}_t is the Kalman gain

$$\mathbf{K}_t = \mathbf{B}_t \mathbf{F}_t^T Q_t^{-1}, \quad (5)$$

with $\mathbf{B}_t = \text{cov}[\boldsymbol{\theta}_t \mid \mathbf{y}_{1:t-1}]$ and $Q_t = \text{var}[y_t \mid \mathbf{y}_{1:t-1}]$ from the Kalman filter in (29) and (30) in Appendix A, respectively. Then $\tilde{\mathbf{x}} = \mathbf{L}^T \mathbf{u}$.

Lemma 2 (Compute $\mathbf{x} = \mathbf{L} \tilde{\mathbf{x}}$ with linear computational cost). *For any N -vector $\tilde{\mathbf{x}}$, let $x_1 = \mathbf{F}_1 \mathbf{b}_1 + Q_1^{1/2} \tilde{x}_1$ and $\tilde{\mathbf{m}}_1 = \mathbf{b}_1 + \mathbf{K}_1 (x_1 - \mathbf{F}_1 \mathbf{b}_1)$. For $t = 2, \dots, N$, iteratively compute x_t by*

$$\mathbf{b}_t = \mathbf{G}_t \tilde{\mathbf{m}}_{t-1}, \quad (6)$$

$$x_t = \mathbf{F}_t \mathbf{b}_t + Q_t^{1/2} \tilde{x}_t, \quad (7)$$

$$\tilde{\mathbf{m}}_t = \mathbf{b}_t + \mathbf{K}_t (x_t - \mathbf{F}_t \mathbf{b}_t), \quad (8)$$

where Q_t and \mathbf{K}_t are from (30) and (5), respectively. Then $\mathbf{x} = \mathbf{L} \tilde{\mathbf{x}}$.

The algorithm in Lemma 1 is unconventional and nontrivial to derive. In comparison, Lemma 2 is directly related to the Kalman filter. To see this, in step (ii) of the Kalman filter given in Appendix A, the one-step-ahead predictive distribution enables computing $\mathbf{L}^{-1} \mathbf{x}$ for any vector \mathbf{x} (Lemma 6). This step is essentially reversed in Lemma 2, which computes $\mathbf{L} \tilde{\mathbf{x}}$ for any vector $\tilde{\mathbf{x}}$, leading to the term *Inverse Kalman filter* (IKF).

Together with Lemma 1 and Lemma 2, the IKF algorithm, outlined in Algorithm 1, reduces the computational operations and storage required for computing $\Sigma \mathbf{u}$ from $\mathcal{O}(N^2)$ to $\mathcal{O}(q^3 N)$ without any approximations. This algorithm applies to all DLMS, including GPs with Matérn kernels of half-integer roughness parameters and one-dimensional inputs. For instance, GPs with Matérn kernels of roughness parameters 0.5 and 2.5 are equivalent to DLMS with $q = 1$ and $q = 3$, respectively. Details are provided in the Supplementary Material.

While Algorithm 1 can be applied to DLM regardless of the noise variance, we do not recommend directly computing $\Sigma \mathbf{u}$ in scenarios when the noise variance V_t is zero or close to zero in Eq. (1).

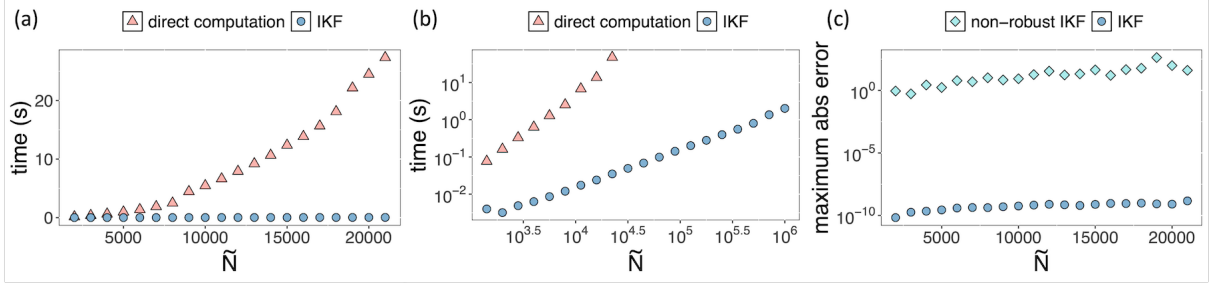


Figure 2: Panels (a) and (b) compare the IKF (blue dots) with direct computation (red triangles) for computing $\Sigma \mathbf{u}$ in the original time scale and logarithmic scale (base 10), respectively. Panel (c) shows the predictive error comparison between non-robust IKF (light blue squares) and robust IKF (blue dots).

Instead, to ensure robustness, we suggest computing $\mathbf{x} = (\Sigma + V\mathbf{I}_N)\mathbf{u}$ with a positive scalar V and outputting $\mathbf{x} - V\mathbf{u}$ as the results of $\Sigma \mathbf{u}$. The result remains exact and independent of the choice of V .

The IKF approach is compared with the direct matrix-vector multiplication of $\Sigma \mathbf{u}$ in noise-free scenarios, focusing on computational time and numerical error (Fig. 2). The experiments utilize $z_t = z(d_t)$ with d uniformly sampled from $[0, 1]$ and the Matérn covariance with a unit variance, roughness parameter being 2.5 and range parameter being $\gamma = 0.1$ [20]. Panels (a) and (b) show that IKF significantly reduces computational costs compared to direct computation, with a linear relationship between computation time and the number of observations. IKF achieves covariance matrix-vector multiplication for a 10^6 -dimensional output vector in about 2 seconds on a desktop. This efficiency is advantageous for iterative algorithms requiring frequent matrix-vector multiplications, including CG algorithm [23] and the randomized log-determinant approximation [43]. Figure 2(c) compares the maximum absolute error between robust IKF with $V = 0.1$ and non-robust IKF with $V = 0$. The non-robust IKF exhibits large numerical errors due to unstable inversion when Q_t , the variance of the one-step-ahead predictive distribution, is close to zero. In contrast, the robust IKF remains stable even with singular or near-singular covariance matrices Σ , as Q_t is always at least V .

Lemmas 1 and 2 motivate the direct connection between each element of the Cholesky factor \mathbf{L} and the parameters in DLMs, and enable the computation of $(\mathbf{L}^T)^{-1}\tilde{\mathbf{x}}$ at a linear computational cost. These results are summarized in Lemmas 3 and 4, respectively, and the proofs of these lemmas are given in Appendix B.

Lemma 3 (Cholesky factor from the inverse Kalman filter). *Denote Cholesky decomposition $\Sigma = \mathbf{L}\mathbf{L}^T$. For any entry (t', t) with $t' \geq t$, we have*

$$L_{t',t} = Q_t^{\frac{1}{2}} \ell_{t',t}, \quad (9)$$

where $\ell_{t',t} = 1$, and for $t' > t$, $\ell_{t',t}$ is defined by

$$\ell_{t',t} = \mathbf{F}_{t'} \left(\prod_{l=t+1}^{t'} \mathbf{G}_l \right) \mathbf{K}_t, \quad (10)$$

with $\prod_{l=t+1}^{t'} \mathbf{G}_l = \mathbf{G}_{t'} \mathbf{G}_{t'-1} \dots \mathbf{G}_{t+1}$, Q_t and \mathbf{K}_t defined in (30) and (5), respectively.

Lemma 4 (Compute $\mathbf{u} = (\mathbf{L}^T)^{-1}\tilde{\mathbf{x}}$ with linear computational cost). For any $\tilde{\mathbf{x}}$, let $u_N = Q_N^{-1/2}\tilde{x}_N$, and $u_{N-1} = Q_{N-1}^{-1/2}\tilde{x}_{N-1} - \ell_{N,N-1}u_N$. For $t = N - 2, \dots, 1$, iteratively compute u_t by

$$u_t = Q_t^{-\frac{1}{2}}\tilde{x}_t - \tilde{\ell}_{t+1,t} - \ell_{t+1,t}u_{t+1}, \quad (11)$$

with $\tilde{\ell}_{t+1,t}$ and $\ell_{t+1,t}$ defined in Lemma 1. Then $\mathbf{u} = (\mathbf{L}^T)^{-1}\tilde{\mathbf{x}}$.

3 Applications

3.1 Nonparametric estimation of particle interaction functions

The motivating example of the IKF approach is estimating interactions between self-driven particles, which is crucial for understanding complex phenomena of molecules and active matter, such as migrating cells and flocking birds. Minimal physical models, such as Vicsek models [52], continuum model [50] and their extensions [3, 13], can explain a wide range of collective motions in both microscopic and macroscopic scales.

Consider a physics model encompassing multiple types of latent interactions. Let \mathbf{y}_i denote the i th observation, a real-valued vector of D_y dimensions, influenced by J distinct interactions, with J being 1 or 2 in practice. For the j th type of interaction, \mathbf{y}_i interacts with a subset, $p_{i,j}$, of particles rather than all particles, typically those within a radius of r_j . This relationship is formally expressed as:

$$\mathbf{y}_i = \sum_{j=1}^J \sum_{k=1}^{p_{i,j}} \mathbf{a}_{i,j,k} z_j(d_{i,j,k}) + \boldsymbol{\epsilon}_i, \quad (12)$$

where $\boldsymbol{\epsilon}_i \sim \mathcal{MN}(0, \sigma_0^2 I_{D_y})$ denotes the Gaussian noise vector, for $i = 1, \dots, n$. The term $\mathbf{a}_{i,j,k}$ is a D_y -dimensional vector of *known* factor loadings, connecting the i th output to the k th neighbor influenced by the j th *unknown* latent interaction $z_j(\cdot)$ at an input $d_{i,j,k}$, such as the distance between particles i and k , for $k = 1, \dots, p_{i,j}$, $i = 1, \dots, n$, and $j = 1, \dots, J$.

Numerous physical and mathematical models of the dynamic behaviors of self-propelled particles can be formulated as in Eq. (12) with a parametric form of a particle interaction function [3, 36]. Nonparametric estimation of particle interactions, on the other hand, is preferred for systems without a known physical mechanism [33, 25, 32], whereas the high computational cost prohibits its direct use for systems involving a large number of particles over a long time.

We employ the DLM to model the latent interaction function. For each interaction type j , we form an input vector $\mathbf{d}_j^{(u)} = [d_{1,j}^{(u)}, \dots, d_{N_j,j}^{(u)}]^T$, where $d_{t,j}^{(u)} = d_{i,j,k}$ with $t = \sum_{i'=1}^{j-1} p_{i',j} + k$ for any tuple (i, j, k) , $k = 1, \dots, p_{i,j}$, $i = 1, \dots, n$, $j = 1, \dots, J$ and $N_j = \sum_{i=1}^n p_{i,j}$. The superscript ‘u’ on $\mathbf{d}_j^{(u)}$ indicates that these inputs are not ordered from the smallest to the largest. We then rearrange $\mathbf{d}_j^{(u)}$ into a non-decreasing input sequence $\mathbf{d}_j = [d_{1,j}, \dots, d_{N_j,j}]^T$ such that $d_{t,j} \leq d_{t',j}$ if $t < t'$, and assume that the latent factor $z_j(d_{t,j})$ follows the DLM framework in Eqs (1)-(2) without a noise, given that the noise has already been defined in Eq. (12).

The marginal distribution of the j th factor model (12) induced by the DLM follows a multivariate normal distribution $\mathbf{z}_j = [z_j(d_{1,j}), \dots, z_j(d_{N_j,j})]^T \sim \mathcal{MN}(\mathbf{0}, \boldsymbol{\Sigma}_j)$. Here, $\boldsymbol{\Sigma}_j$ is an $N_j \times N_j$ covariance matrix, with the (t, t') th entry being $\text{cov}[z_j(d_{t,j}), z_j(d_{t',j})] = \sigma_j^2 c_j(d_{t,j}, d_{t',j}) = \sigma_j^2 c_j(d)$, where σ_j^2 is the variance parameter, $c_j(\cdot)$ is the correlation function, and $d = |d_{t,j} - d_{t',j}|$. Given the smooth nature of interaction functions, we use the Matérn correlation with a half-integer roughness parameter ν_j [20]. For $\nu_j = 0.5$, the Matérn correlation simplifies to the exponential kernel,

$c_j(d) = \exp(-d/\gamma_j)$ with the range parameter γ_j . For $\nu_j = 2.5$, Matérn correlation follows:

$$c_j(d) = \left(1 + \frac{5^{1/2}d}{\gamma_j} + \frac{5d^2}{3\gamma_j^2}\right) \exp\left(-\frac{5^{1/2}d}{\gamma_j}\right). \quad (13)$$

A Gaussian process with Matérn correlation is $\lceil \nu_j - 1 \rceil$ mean squared differentiable [42], allowing direct control over process smoothness through ν_j , an appealing feature as the smoothness of the process is directly controlled by ν_j .

By integrating out latent factor processes \mathbf{z}_j , the marginal distribution of the observation vector $\mathbf{y} = (\mathbf{y}_1^T, \dots, \mathbf{y}_n^T)^T$ with dimension $\tilde{N} = nD_y$ follows a multivariate normal distribution:

$$\left(\mathbf{y} \mid \boldsymbol{\Sigma}_j^{(u)}, \sigma_0^2\right) \sim \mathcal{MN}\left(\mathbf{0}, \sum_{j=1}^J \mathbf{A}_j \boldsymbol{\Sigma}_j^{(u)} \mathbf{A}_j^T + \sigma_0^2 \mathbf{I}_{\tilde{N}}\right), \quad (14)$$

where \mathbf{A}_j is an $\tilde{N} \times N_j$ sparse block diagonal matrix, such that the i th diagonal block is a $D_y \times p_{i,j}$ matrix $\mathbf{A}_{i,j} = [\mathbf{a}_{i,j,1}, \dots, \mathbf{a}_{i,j,p_{i,j}}]$ for $i = 1, \dots, n$, and $\boldsymbol{\Sigma}_j^{(u)}$ is an $N_j \times N_j$ covariance matrix induced by the unordered inputs with $\boldsymbol{\Sigma}_j^{(u)}(t, t') = \text{cov}\left[z_j(d_{t,j}^{(u)}), z_j(d_{t',j}^{(u)})\right]$ for any $1 \leq t, t' \leq N_j$, for $j = 1, \dots, J$. This covariance $\boldsymbol{\Sigma}_j^{(u)}$ differs from the covariance matrix of ordered inputs $\boldsymbol{\Sigma}_j$, adding an extra layer of algorithmic complexity.

Integrating out the latent factor $z(\cdot)$, the posterior predictive distribution of the latent variable $z_j(d^*)$ for any given input d^* follows a normal distribution

$$(z_j(d^*) \mid \mathbf{y}, \sigma_0^2, \boldsymbol{\sigma}^2, \boldsymbol{\gamma}, \mathbf{r}) \sim \mathcal{N}(\hat{z}_j(d^*), c_j^*(d^*)), \quad (15)$$

where the predictive mean and variance are

$$\hat{z}_j(d^*) = \boldsymbol{\Sigma}_j^{(u)}(d^*)^T \mathbf{A}_j^T \boldsymbol{\Sigma}_y^{-1} \mathbf{y}, \quad (16)$$

$$c_j^*(d^*) = c_j(d^*, d^*) - \boldsymbol{\Sigma}_j^{(u)}(d^*)^T \mathbf{A}_j^T \boldsymbol{\Sigma}_y^{-1} \mathbf{A}_j \boldsymbol{\Sigma}_j^{(u)}(d^*), \quad (17)$$

with $\boldsymbol{\Sigma}_y = \sum_{j=1}^J \mathbf{A}_j \boldsymbol{\Sigma}_j^{(u)} \mathbf{A}_j^T + \sigma_0^2 \mathbf{I}_{\tilde{N}}$ and $\boldsymbol{\Sigma}_j^{(u)}(d^*) = [c_j(d_{1,j}^{(u)}, d^*), \dots, c_j(d_{N_j,j}^{(u)}, d^*)]^T$.

The main computational challenge for calculating the predictive distribution (15) lies in inverting the covariance matrix $\boldsymbol{\Sigma}_y = \sum_{j=1}^J \mathbf{A}_j \boldsymbol{\Sigma}_j^{(u)} \mathbf{A}_j^T + \sigma_0^2 \mathbf{I}_{\tilde{N}}$, where \tilde{N} and N_j range between 10^5 and 10^6 in applications. Although various approximation approaches of GPs have been proposed [51, 45, 12, 4, 30, 15, 5, 26], they typically approximate a model with a parametric covariance $\boldsymbol{\Sigma}_j$, rather than $\boldsymbol{\Sigma}_y$, thus not directly applicable for computing the distribution in (15).

We combine the IKF with the CG algorithm [23] to accelerate computing the predictive distribution. The resulting new method, termed IKF-CG, computes $\boldsymbol{\Sigma}_y^{-1} \mathbf{y}$ via CG iterations, where each step involves matrix multiplication of $\boldsymbol{\Sigma}_y \mathbf{u}$ for an \tilde{N} -dimensional vector \mathbf{u} , which is substantially accelerated by the IKF algorithm. Our method reduces the computational cost from increasing cubically fast along with the number of observations to a pseudolinear order with respect to the number of latent states. Details on computing the predictive mean and variance are provided in Appendix C. The IKF-CG algorithm can be utilized for parameter estimation through both cross-validation and maximum likelihood estimation, with the latter requiring an additional approximation of the logarithm of the determinant [43]. These methods are elaborated in Appendix D, with the computational complexity discussed in Appendix E. The CG algorithm is summarized in the Supplementary Material.

3.2 Predicting incomplete lattice of correlated data

Missing values in lattice data are ubiquitous in scientific datasets, such as satellite radar interferograms [1] and temperature measurements [49]. Here, we utilize the IKF-CG algorithm to accelerate the computation of predicting incomplete data. Consider \tilde{N} observations modeled by $\mathbf{y} = \mathbf{A}\mathbf{z} + \boldsymbol{\epsilon}$, where \mathbf{z} is an N -dimensional latent mean vector on a 2D lattice, \mathbf{A} is an $\tilde{N} \times N$ matrix of \tilde{N} 1s and $N\tilde{N} - \tilde{N}$ 0s by mapping the latent vector to the observations, and the Gaussian noise vector follows $\boldsymbol{\epsilon} \sim \mathcal{MN}(\mathbf{0}, \sigma_0^2 \mathbf{I}_{\tilde{N}})$.

For demonstration purposes, we consider modeling an N -vector of observations by $\mathbf{z} \sim \mathcal{MN}(\mathbf{0}, \boldsymbol{\Sigma})$, where $\boldsymbol{\Sigma} = \sigma^2 \mathbf{R}_1 \otimes \mathbf{R}_2$, with \mathbf{R}_1 and \mathbf{R}_2 being the $n_1 \times n_1$ and $n_2 \times n_2$ correlation matrices of input variables s_1 and s_2 of the lattice, respectively, $N = n_1 \times n_2$, and \otimes denotes the Kronecker product. Each of \mathbf{R}_1 and \mathbf{R}_2 is parameterized by a correlation function, such as the Matérn correlation. This application can be extended to models with semi-separable or non-separable covariances, and distinct mean patterns [17]. After integrating out the latent factors \mathbf{z} , the marginal distribution of \mathbf{y} follows

$$(\mathbf{y} \mid \boldsymbol{\Sigma}, \sigma_0^2) \sim \mathcal{MN}(\mathbf{0}, \mathbf{A}\boldsymbol{\Sigma}\mathbf{A}^T + \sigma_0^2 \mathbf{I}_{\tilde{N}}). \quad (18)$$

Given the observed data, the posterior distribution of \mathbf{z} is a multivariate normal distribution with mean $\hat{\mathbf{z}}$ given by

$$\hat{\mathbf{z}} = \boldsymbol{\Sigma}\mathbf{A}^T \boldsymbol{\Sigma}_y^{-1} \mathbf{y}, \quad (19)$$

where $\boldsymbol{\Sigma}_y = \mathbf{A}\boldsymbol{\Sigma}\mathbf{A}^T + \sigma_0^2 \mathbf{I}_{\tilde{N}}$. We use the IKF-CG algorithm to calculate the predictive mean. In each iteration of the CG algorithm, we need to compute $\boldsymbol{\Sigma}\mathbf{u} = (\mathbf{R}_1 \otimes \mathbf{R}_2)\mathbf{u} = \text{vec}(\mathbf{R}_2 \mathbf{U} \mathbf{R}_1)$, where $\text{vec}(\mathbf{U}) = \mathbf{u}$, with $\text{vec}(\cdot)$ being the vectorization operator. Each matrix-matrix multiplication can be significantly accelerated by the IKF algorithm, reducing the computational cost to $\mathcal{O}(q^3 N)$ when we use a DLM-induced covariance with q latent states for both inputs. Details of parameter estimation are provided in Appendix D.

4 Numerical results of estimating particle interaction functions

4.1 Evaluation criteria

We start with presenting the numerical results from the simulated studies in Section 4.2-4.3 and the real data analysis in Section 4.4 for the nonparametric estimation of particle interaction functions in physical models. In the simulations, observations are generated at equally spaced time frames $\tau = 1, \dots, T$ with a time interval of h , though our approach is applicable to both equally and unequally spaced time frames. In addition, the number of particles, n_τ , is assumed to be constant at each time frame during simulations.

For each of the J latent factors, predictive performance is assessed using normalized root mean squared error (NRMSE $_j$), the average length of the 95% posterior credible interval ($L_j(95\%)$), and the proportion of interaction function values covered within the 95% posterior credible interval

($P_j(95\%)$), based on n^* test inputs $\mathbf{d}_j^* = (d_{1,j}^*, \dots, d_{n^*,j}^*)^T$:

$$\text{NRMSE}_j = \left(\frac{\sum_{i=1}^{n^*} (\hat{z}_j(d_{i,j}^*) - z_j(d_{i,j}^*))^2}{\sum_{i=1}^{n^*} (\bar{z}_j - z_j(d_{i,j}^*))^2} \right)^{1/2}, \quad (20)$$

$$L_j(95\%) = \frac{1}{n^*} \sum_{i=1}^{n^*} \text{length} \{CI_{i,j}(95\%)\}, \quad (21)$$

$$P_j(95\%) = \frac{1}{n^*} \sum_{i=1}^{n^*} 1_{z_j(d_{i,j}^*) \in CI_{i,j}(95\%)}. \quad (22)$$

Here, $\hat{z}_j(d_{i,j}^*)$ represents the prediction at $d_{i,j}^*$, \bar{z}_j is the average of the j th interaction function evaluated on \mathbf{d}_j^* , and $CI_{i,j}(95\%)$ denotes the 95% posterior credible interval of $z_j(d_{i,j}^*)$, for $j = 1, \dots, J$. A desirable method should exhibit a relatively small NRMSE, a short average length of the credible interval, and a coverage proportion of the test sample close to 95%.

To account for variability due to initial particle positions, velocities, and noise, each simulation scenario is repeated $E = 20$ times, and the average of the quantities for each criterion is computed. Unless otherwise specified, parameters are estimated by cross-validation discussed in Appendix D, with 20% of the dataset used as validation set and the rest 80% as the training set. The scalability and accuracy of the algorithm in computing the posterior mean and the likelihood function are examined in Section 4.2. All computations are performed on a macOS Mojave system with an 8-core Intel i9 processor running at 3.60 GHz and 32 GB of RAM.

4.2 Vicsek model

We first consider the Vicsek model, a seminal framework for studying collective motion [52]. Let $\mathbf{y}_k(\tau) = (y_{k,1}(\tau), y_{k,2}(\tau))^T$ denote the 2D velocity of the k th particle at time τ , where $y_{k,1}(\tau)$ and $y_{k,2}(\tau)$ represent the velocity components along two orthogonal directions, for $k = 1, \dots, n_\tau$ and $\tau = 1, \dots, T$. The velocity magnitude is a constant $v = \|\mathbf{y}_k(\tau)\|$, with $\|\cdot\|$ denoting the L_2 norm. The velocity angle $\phi_k(\tau) = \tan^{-1}(y_{k,2}(\tau)/y_{k,1}(\tau))$ is updated as

$$\phi_k(\tau) = \frac{1}{p_k(\tau-1)} \sum_{k' \in ne_k(\tau-1)} \phi_{k'}(\tau-1) + \epsilon_k(\tau), \quad (23)$$

where $\epsilon_k(\tau)$ is a zero-mean Gaussian noise with variance σ_0^2 . The set of neighboring particles, $ne_k(\tau-1)$, includes those within a radius of r from particle k at time $\tau-1$, i.e., $ne_k(\tau-1) = \{k' : \|\mathbf{s}_{k'}(\tau-1) - \mathbf{s}_k(\tau-1)\| < r\}$, where $\mathbf{s}_k(\tau-1)$ and $\mathbf{s}_{k'}(\tau-1)$ are 2D position vectors of particle k and its neighbor k' , respectively, and $p_k(\tau-1)$ is the number of neighboring particles of the k th particle including itself at time $\tau-1$. The position of particle k at time τ is updated as:

$$\mathbf{s}_k(\tau) = \mathbf{s}_k(\tau-1) + v[\cos(\phi_k(\tau)), \sin(\phi_k(\tau))]^T h, \quad k = 1, \dots, n_\tau. \quad (24)$$

The particle interaction function in Eq. (23) can be represented as a latent factor model in Eq. (12) with a linear interaction function $z(d) = d$ for $d = \phi_{k'}(\tau-1)$ for neighboring particle k' and a coefficient of $1/p_k(\tau-1)$ for the k th particle at time $\tau-1$. The interaction function is estimated nonparametrically without assuming linearity. The dependence on j is omitted here as the Vicsek model only has one type of interaction. In simulations, the initial velocity of the particles is set to be $[v \cos(\phi_k(0)), v \sin(\phi_k(0))]^T$, with ϕ_k uniformly drawn from $\text{Unif}[0, 2\pi]$ and $v = 2^{1/2}/2 \approx 0.71$. Initial positions are uniformly sampled from $[0, n_\tau^{1/2}] \times [0, n_\tau^{1/2}]$ to keep consistent particle density

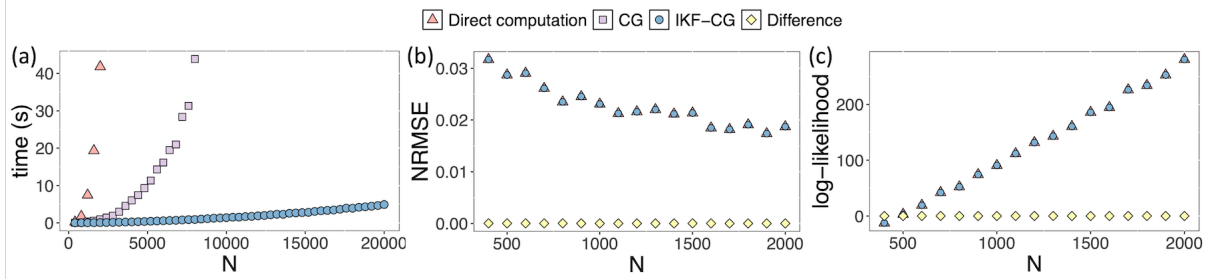


Figure 3: Panel (a) displays the computational time of calculating the predictive mean with the IKF-CG algorithm (blue dots), CG method (purple squares), and direct computation (red triangles) for the Vicsek model with different numbers of observations. Panel (b) and (c) show the NRMSE of the predictive mean of the interaction function and log-likelihood from the direct computation (red triangles) and the IKF-CG algorithm (blue dots), respectively. The difference in NRMSE, shown in yellow diamonds, is on the order of 10^{-5} to 10^{-4} , and the difference in log-likelihood is on the order of 10^{-4} to 10^{-3} .

across experiments. The interaction radius $r = 0.5$ is estimated alongside other parameters, with results detailed in the Supplementary Material.

We first compare the computational cost and accuracy of IKF-CG, CG, and direct computation, for calculating the predictive mean in Eq. (16) and the marginal likelihood in Eq. (14) with a Matérn covariance using the roughness parameter 2.5 in Eq. (13). Simulations are conducted with $n_\tau = 100$ particles and noise variance of $\sigma_0^2 = 0.2$ at varying simulation times T . Panel (a) of Fig. 3 records the computational time of calculating $n^* = 100$ testing inputs for simulation times T ranging from 4 to 200. Direct computation, involving forming and inverting the covariance matrix, incurs the highest computational cost. The CG algorithm, while more scalable, still involves significant matrix-vector multiplication costs. The IKF-CG approach outperforms both methods, as the matrix-vector multiplication costs only $\mathcal{O}(q^3N)$ operations in IKF. Figure 3(b) compares the NRMSE of the predictive mean between direct computation and IKF-CG for observation numbers ranging from 400 to 2,000, corresponding to T ranging from 4 to 20. Both methods yield nearly identical predictive error, with the NRMSE difference being negligible. In Fig. 3(c), we compare the direct computation of the log-likelihood with the IKF-CG using the log determinant approximation discussed in Appendix D. Both methods produce similar log-likelihood values across different sample sizes.

Next, we evaluate the performance of the IKF-CG algorithm across 12 scenarios with varying particle numbers ($n_\tau = 100, 300, 900$), time frames ($T = 5, 10$), and noise variances ($\sigma_0^2 = 0.1, 0.2$). The predictive performance is evaluated using $n^* = 200$ test inputs evenly spaced across the domain of the interaction function, $[-\pi, \pi]$. The evaluation metrics (20)-(22) are averaged over $E = 20$ experiments.

Panels (a) and (b) of Figs. 4-5 display the predictive performance of the particle interaction having the Matérn covariance with the roughness parameters being 2.5 and the exponential covariance, respectively. The results show low NRMSEs in all scenarios, with improved accuracy for larger datasets and smaller noise variances. The decrease in the average length of 95% posterior interval with increasing sample size, along with the relatively small span of the interval compared to the output range $[-\pi, \pi]$, highlights improved prediction confidence with more observations. Moreover, the coverage proportion of the latent interaction function within the 95% posterior credible is close to the nominal 95% level in all cases, validating the reliability of the uncertainty quantification.

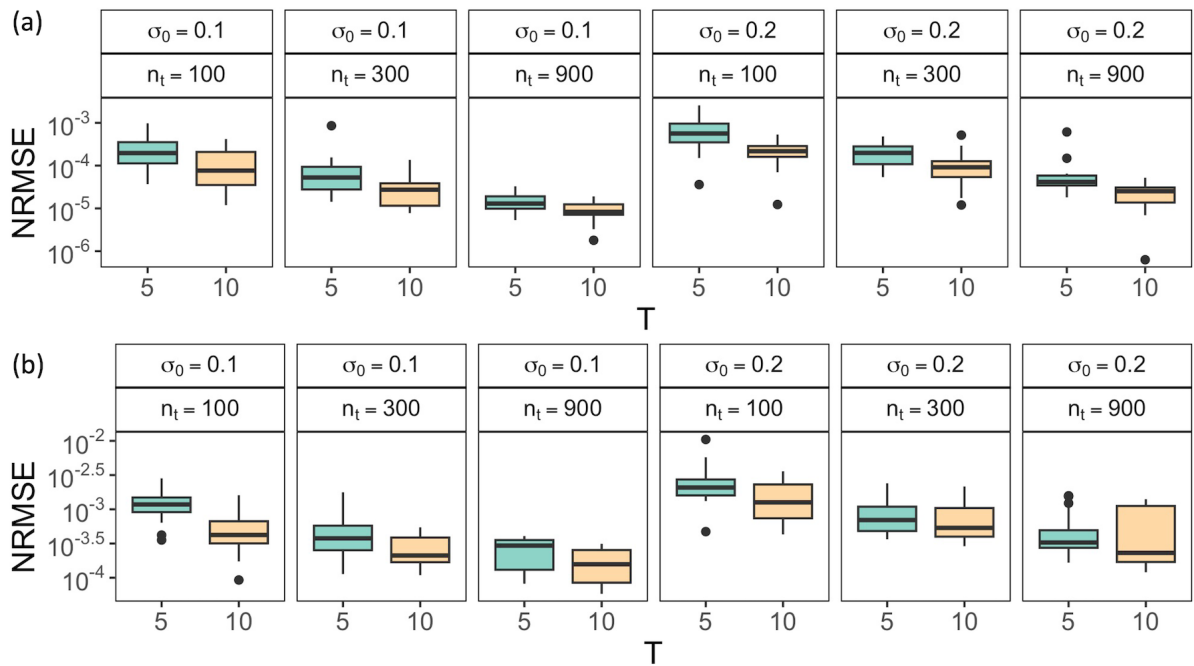


Figure 4: Boxplots of NRMSE in (20) for estimating the latent interaction function in the Vicsek model. The results are based on 20 experiments for each scenario, using the Matérn covariance with roughness parameter 2.5 (Panel (a)) and exponential covariance (Panel (b)).

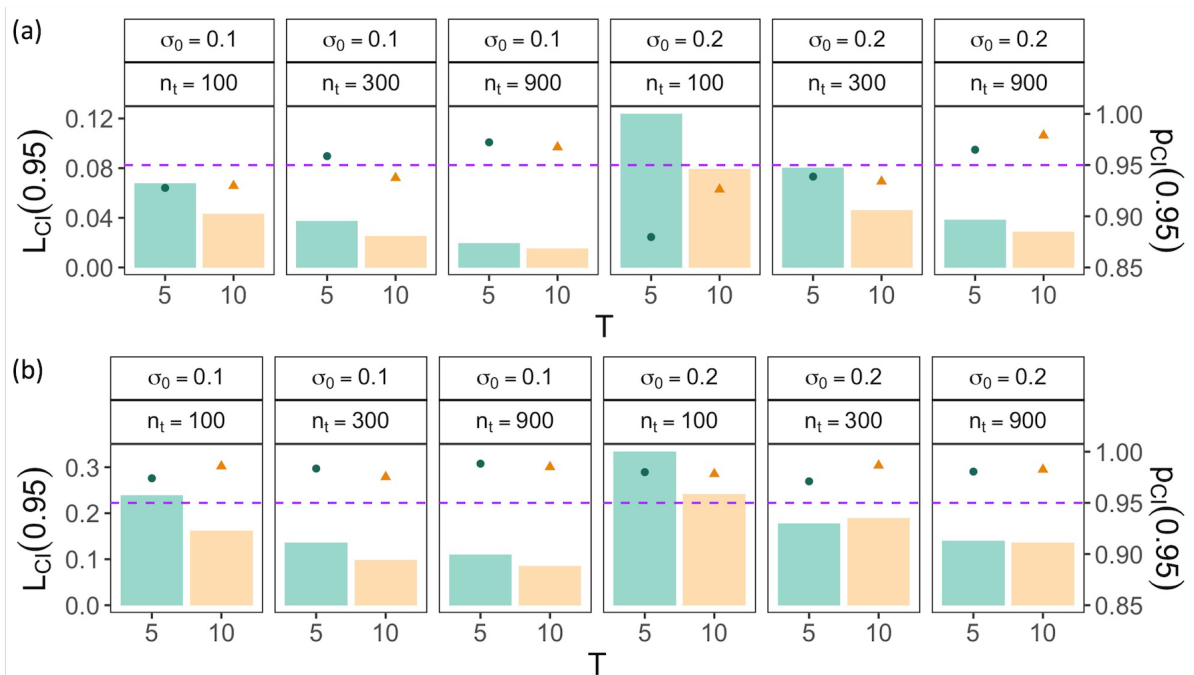


Figure 5: Uncertainty assessment of the predicted interaction function of the Vicsek model using the Matérn covariance function with roughness parameter 2.5 (Panel (a)) and using exponential covariance function (Panel (b)). The bars represent the mean of the 95% posterior credible interval length computed by Eq. (21) over 20 experiments, and the dots represent the mean of the 95% coverage proportion computed by Eq. (22) over 20 experiments. The purple dashed line is 0.95, indicating the optimal value of coverage $P(95\%)$ for the dots.

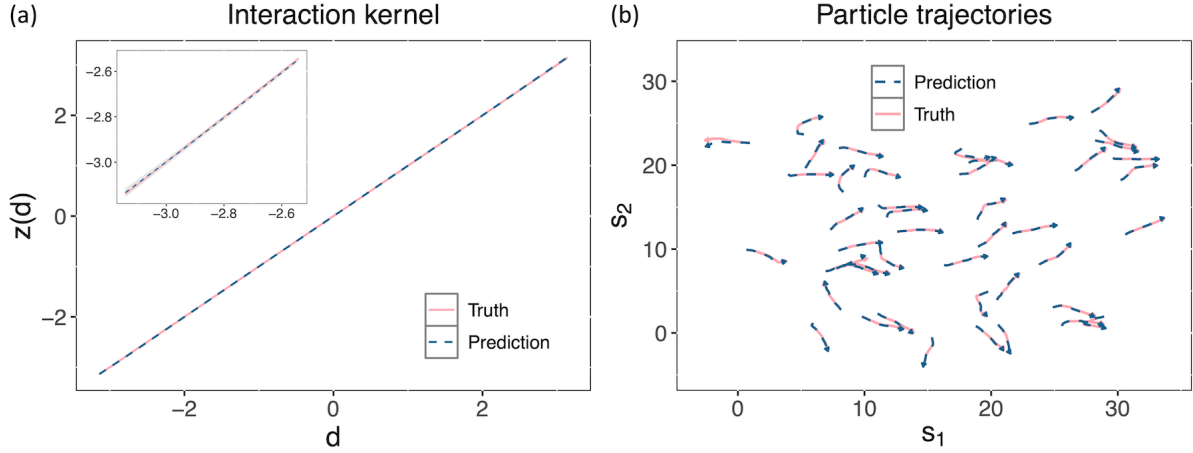


Figure 6: Panel (a) displays the prediction of the interaction function (blue dashed lines), the truth (pink solid lines), and the 95% posterior credible interval (grey shaded area) for the Vicsek model with $n_\tau = 900$, $T = 10$, and $\sigma_0 = 0.1$, using Matérn covariance function with roughness parameter 2.5. Panel (b) shows the forecast of the particle trajectory of sampled 45 particles over 50 time frames using the estimated function (blue dashed lines) and the true interaction function (pink solid lines), with identical noise samples for both truth and predictions.

From Figs. 4-5, we find that the model with the Matérn covariance in Eq. (13) yields lower NRMSE and shorter 95% posterior credible intervals than the exponential kernel. This is because the latent process with Eq. (13) is twice mean squared differentiable, inducing a smoother prior over the interaction function space compared to the exponential kernel.

Figure 6(a) compares the predicted and true interaction function over the input domain $[-\pi, \pi]$, demonstrating high agreement. The 95% interval is narrow yet covers approximately 95% of the test samples of the interaction function. Figure 6(b) displays the trajectories of simulated particles over $T^* = 50$ time steps using the predicted mean for one-step-ahead predictions and true interaction function. The trajectories, with identical initial positions and noise samples, are visually similar.

4.3 A modified Vicsek model with multiple interactions

Various extensions of the Vicsek model have been studied [3, 13]. For illustration purposes, we consider a modified version of the Vicsek model that incorporates two interaction functions. The 2D velocity of the k th particle at time τ , denoted as $\mathbf{y}_k(\tau) = (y_{k,1}(\tau), y_{k,2}(\tau))^T$, is governed by two types of interactions:

$$\mathbf{y}_k(\tau) = \frac{\sum_{k' \in ne_k(\tau-1)} \mathbf{y}_{k'}(\tau-1)}{p_k(\tau-1)} + \frac{\sum_{k' \in ne'_k(\tau-1)} f(d_{k,k'}(\tau-1)) \mathbf{e}_{k,k'}(\tau-1)}{p'_k(\tau-1)} + \boldsymbol{\epsilon}_k(\tau), \quad (25)$$

where the second interaction is $f(d_{k,k'}(\tau-1)) = -2(5(d_{k,k'}(\tau-1) + 0.01))^{-1} + 20d_{k,k'}(\tau-1) - 15.5$ with $d_{k,k'}(\tau-1) = \|\mathbf{s}_k(\tau-1) - \mathbf{s}_{k'}(\tau-1)\|$, $\mathbf{e}_{k,k'}(\tau-1) = (\mathbf{s}_k(\tau-1) - \mathbf{s}_{k'}(\tau-1))/d_{k,k'}(\tau-1)$, $\boldsymbol{\epsilon}_k(\tau) = (\epsilon_{k,1}(\tau), \epsilon_{k,2}(\tau))^T$ is a Gaussian noise vector with variance σ_0^2 , $p_k(\tau-1)$ and $p'_k(\tau-1)$ are the number of neighbors of the k th particle at time $\tau-1$ in two types of interactions.

The modified Vicsek model in Eq. (25) can be represented as a latent factor model in Eq. (12) with two latent interactions. The first interaction aligns the velocity of a particle linearly with its neighbors, including itself, defined as $ne_k(\tau-1) = \{k' : \|\mathbf{s}_{k'}(\tau-1) - \mathbf{s}_k(\tau-1)\| < r\}$, with $p_k(\tau-1)$ being the number of neighbors. The second interaction, $f(\cdot)$, models repulsion at

close distances and attraction at longer distances, involving neighbors excluding the particle itself, defined as $ne'_k(\tau - 1) = \{k' : \|\mathbf{s}_{k'}(\tau - 1) - \mathbf{s}_k(\tau - 1)\| < r \text{ and } k \neq k'\}$. A common interaction radius $r = 0.5$ is assumed for both interactions.

		$\sigma_0 = 0.1$						
		First Interaction			Second Interaction			
		NRMSE	$L_1(0.95)$	$P_1(0.95)$	NRMSE	$L_2(0.95)$	$P_2(0.95)$	
$n_\tau = 100$	$T = 5$	6.8×10^{-3}	0.098	92%	8.7×10^{-2}	0.29	94%	
	$T = 10$	6.0×10^{-3}	0.097	95%	3.8×10^{-2}	0.18	96%	
$n_\tau = 300$	$T = 5$	1.2×10^{-2}	0.23	87%	3.2×10^{-2}	0.21	96%	
	$T = 10$	4.2×10^{-3}	0.10	98%	2.0×10^{-2}	0.13	97%	
$n_\tau = 900$	$T = 5$	5.6×10^{-3}	0.10	96%	1.4×10^{-2}	0.12	98%	
	$T = 10$	4.4×10^{-3}	0.12	97%	1.4×10^{-2}	0.10	96%	
		$\sigma_0 = 0.2$						
		First Interaction			Second Interaction			
		NRMSE	$L_1(0.95)$	$P_1(0.95)$	NRMSE	$L_2(0.95)$	$P_2(0.95)$	
$n_\tau = 100$	$T = 5$	9.9×10^{-3}	0.16	98%	1.6×10^{-1}	0.45	93%	
	$T = 10$	8.9×10^{-3}	0.19	94%	1.0×10^{-1}	0.37	94%	
$n_\tau = 300$	$T = 5$	9.7×10^{-3}	0.23	98%	4.8×10^{-2}	0.31	97%	
	$T = 10$	9.2×10^{-3}	0.22	96%	3.5×10^{-2}	0.22	96%	
$n_\tau = 900$	$T = 5$	6.2×10^{-3}	0.19	100%	2.5×10^{-2}	0.21	99%	
	$T = 10$	7.3×10^{-3}	0.23	99%	2.0×10^{-2}	0.18	99%	

Table 1: The predictive accuracy and uncertainty assessment by (20)-(22) for the modified Vicsek model with Matérn covariance function and roughness parameter 2.5.

We simulate 12 scenarios, each replicated $E = 20$ times, using the same number of particles, time frame, and noise level as in the original Vicsek model in Section 4.2. The predictive performance of the latent factor model is evaluated using $n^* = 200$ testing inputs evenly spaced across the training input domain of each interaction function. We focus on the model with the Matérn kernel in Eq. (13) and results with the exponential kernel are detailed in the Supplementary Material. Consistent with the results of the Vicsek model, we find models with the Matérn kernel in Eq. (13) are more accurate due to the smooth prior imposed on the interaction function.

Table 1 presents the predictive performance of the model. While the NRMSEs of both interaction functions are relatively small, the NRMSE for the second interaction function, which accounts for repulsion, is higher than that for the first, due to fewer samples with a close-proximity neighbor, leading to less accurate predictions. Increasing the number of observations mitigates this issue, as evidenced in Table 1. The average length of the 95% posterior credible interval for the second interaction decreases with larger sample size, and the proportion of samples covered by the interval is close to the 95% nominal level, regardless of the size of the training dataset.

In Fig. 7, we show the predictions of the two interaction functions, where the shaded region represents the 95% posterior credible interval. These predictions closely match the true values, and the 95% intervals, while narrow compared to the output range and nearly invisible in the plots, mostly cover the truth. This suggests a high degree of confidence in predictions.

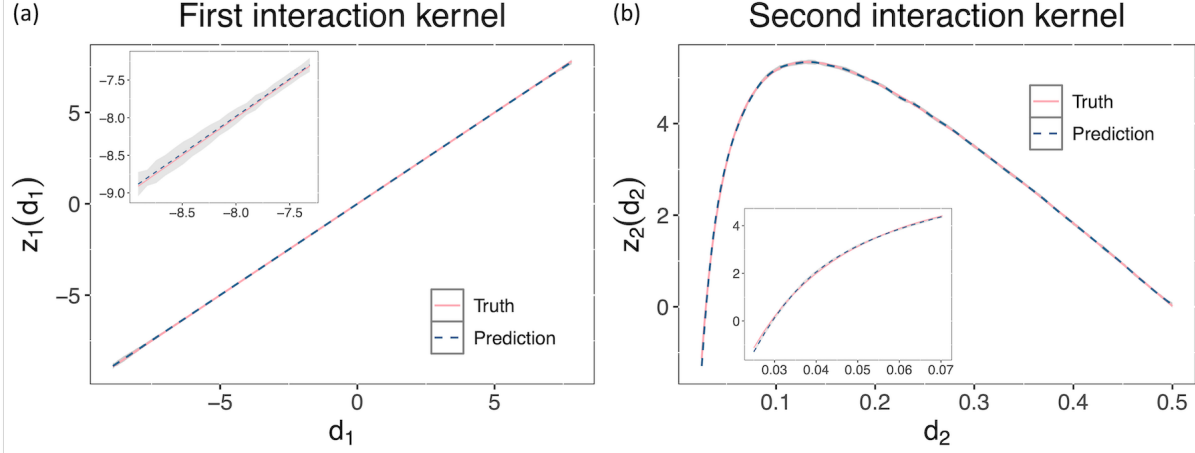


Figure 7: Predictions of two particle interaction functions (blue dashed curves), truth (pink solid curves), and the 95% posterior credible interval (shaded region) for the first experiment when $n_\tau = 900$, $T = 10$, and $\sigma_0 = 0.1$.

4.4 Estimating cell-cell interactions on anisotropic substrates

We analyze the video microscopy data collected by [34], which contains trajectories of over 2,000 human dermal fibroblasts moving on a substrate with nematic order aligned horizontally. This experiment, designed to guide cellular alignment by an anisotropic, liquid-crystalline aligned substrate, shows increasing alignment order of cells over time, although the underlying mechanism remains largely unknown. The cells were imaged every 20 minutes for around 36 hours, with cell counts growing from 2,615 to 2,953 due to proliferation. Our goal is to estimate the latent interaction function between cells. Given the vast number of velocity observations ($\tilde{N} \approx 300,000$), directly forming and inverting the covariance matrix is impractical.

We apply the IKF-CG algorithm to estimate the latent interaction function between cells. Due to the anisotropic substrate, cellular motions differ in magnitude between vertical and horizontal directions. We independently model the velocities of the k th cell in each direction l by

$$y_{k,l}(\tau) = \frac{1}{p_{ne_{k,l}(\tau-1)}} \sum_{k' \in ne_{k,l}(\tau-1)} z_l(d_{k',l}) + \epsilon_{k,l}(\tau), \quad k = 1, \dots, n_\tau \quad (26)$$

where n_τ is the cell count at time frame τ , $l = 1, 2$ for horizontal and vertical directions, respectively, and $\epsilon_{k,l}(\tau) \sim \mathcal{N}(0, \sigma_{0,l}^2(\tau))$ denotes the noise. Inspired by the modified Vicsek model, we set $d_{k',l} = y_{k',l}(\tau - 1)$. To reflect the velocity decrease over time due to increasing cell confluence, we define $\sigma_{0,l}^2(\tau) = \omega_l \sigma_{v,l}^2(\tau - 1)$, where $\sigma_{v,l}^2(\tau - 1)$ is the sample variance of velocity at the $(\tau - 1)$ th time frame, and ω_l is a parameter estimated by data, for $l = 1, 2$. The neighboring set excludes the cells moving in opposite directions, $ne_{k,l}(\tau - 1) = \{k' : \|\mathbf{s}_{k'}(\tau - 1) - \mathbf{s}_k(\tau - 1)\| < r_l \text{ and } \mathbf{y}_k(\tau - 1) \cdot \mathbf{y}_{k'}(\tau - 1) > 0\}$ for $l = 1, 2$, to reflect the observed behavior of cells gliding and intercalating [53].

We use observations from the first half of the time frames as the training dataset and the latter half as the testing set. The predicted interaction function in Fig. 8 shows that the estimated effect diminishes in both directions due to cell-substrate interaction, such as friction. The estimated uncertainty increases when the absolute input velocity of neighboring particles in the previous time frame is large, attributed to fewer observations at the boundary of the input region. Furthermore, the interaction in the vertical direction is smaller than in the horizontal direction, owing to the confinement from the substrate in the vertical direction.

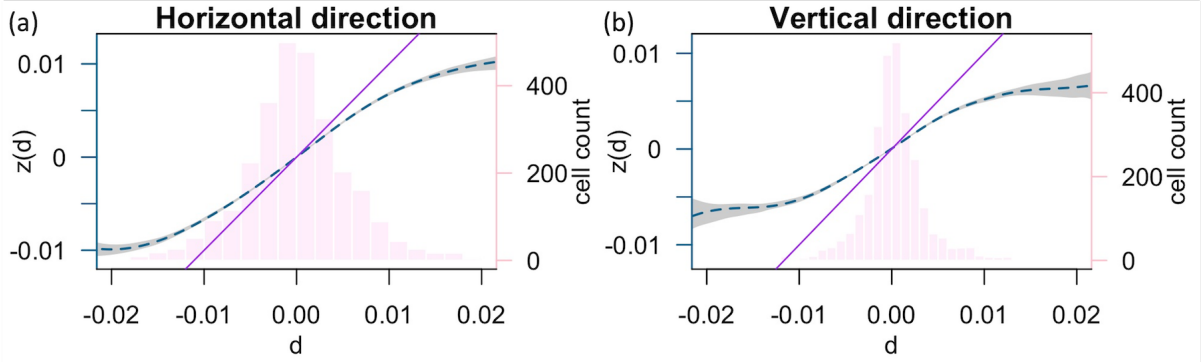


Figure 8: The blue dashed curve shows the predicted interaction function for the horizontal direction (panel (a)) and the vertical direction (panel (b)), and the grey shaded area represents the 95% credible interval. The purple straight line of slope 1 represents the prediction using the Vicsek model. The light pink histogram shows the velocity distribution at a selected time frame.

Our nonparametric estimation approach of the interaction function is compared with two models for one-step-ahead forecasts of directional velocities, including the original Vicsek model, where the velocity magnitude is fixed while the angle is updated (Section 4.2), and the anisotropic Vicsek model, which predicts the current velocity using the average velocity of neighboring cells from the previous time frame. As shown in Table 2, our model outperforms both Vicsek models in RMSE for the one-step forecast of directional velocities, despite the large inherent stochasticity in cellular motion. Furthermore, our proposed latent factor model closely matches the nominal 95% coverage for test velocities, with notably shorter average interval lengths than the anisotropic Vicsek model. These findings underscore the effectiveness of the IFK algorithm, which enables the use of large amount of data to overcome large stochasticity in data for capturing the underlying dynamics of alignment processes.

	Horizontal direction			Vertical direction		
	RMSE	L(95%)	P(95%)	RMSE	L(95%)	P(95%)
Baseline Vicsek	4.5×10^{-3}	0.011	80%	5.3×10^{-3}	0.011	95%
Anisotropic Vicsek	3.9×10^{-3}	0.024	98%	2.6×10^{-3}	0.020	99%
Nonparametric estimation	3.5×10^{-3}	0.015	94%	2.3×10^{-3}	0.0092	94%

Table 2: One-step ahead prediction performance on the testing dataset. Here $\text{RMSE} = \{\sum_{\tau=1}^{T^*} \sum_{k=1}^{n_{\tau}} (\hat{y}_{k,l}(\tau) - y_{k,l}(\tau))^2 / \sum_{\tau=1}^{T^*} n_{\tau}\}^{1/2}$, with T^* denoting the number of testing time frames. The values of L(95%) and P(95%) are computed similarly as in Eqs. (21) - (22), but with the predictive interval of z replaced by that of y .

5 Numerical results of predicting incomplete lattice data

5.1 Evaluation criteria

In this section, we present the results of a simulated study in Section 5.2 and a real data analysis in Section 5.3 for predicting incomplete lattices of correlated data. The NRMSE is used to evaluate the predictive performance of the missing regions. Similar to the definition of observation \mathbf{y} in Section 3.2, the $N - \tilde{N}$ dimensional vector of missing entries is modeled by $\mathbf{y}^{(m)} = \mathbf{A}^{(m)} \mathbf{z} + \boldsymbol{\epsilon}^{(m)}$,

where $\mathbf{A}^{(m)} \in \mathbb{R}^{(N-\tilde{N}) \times N}$ has $(N - \tilde{N})$ 1s, with all other entries being 0s to map the latent vector to the missing values, and $\boldsymbol{\epsilon}^{(m)}$ is a Gaussian noise vector with variance σ_0^2 . The simulated mean of the missing region is $\mathbf{z}^{(m)} = \mathbf{A}^{(m)}\mathbf{z}$ and the predicted values of the missing region are denoted as $\hat{\mathbf{z}}^{(m)} = \mathbf{A}^{(m)}\hat{\mathbf{z}}$. The NRMSE is defined as

$$\text{NRMSE} = \left(\frac{\sum_{i=1}^{N-\tilde{N}} (\hat{z}_i^{(m)} - z_i^{(m)})^2}{\sum_{i=1}^N (\bar{z} - z_i)^2} \right)^{1/2}, \quad (27)$$

where $\hat{z}_i^{(m)}$, $z_i^{(m)}$, and z_i represent the i th entry of $\hat{\mathbf{z}}^{(m)}$, $\mathbf{z}^{(m)}$, and \mathbf{z} , respectively, and \bar{z} is the mean of the vector \mathbf{z} . Since for real data, the underlying true \mathbf{z} is unknown, the NRMSE in real data analysis in Section 5.3 is computed as in Eq. (27) with $\hat{z}_i^{(m)}$, $z_i^{(m)}$, and \bar{z} replaced by $y_i^{(m)}$, y_i , and \bar{y} , representing the i th entry of $\mathbf{y}^{(m)}$, \mathbf{y} and the average of $[\mathbf{y}^{(m)}, \mathbf{y}]$, respectively.

Our IKF-CG approach is compared with four popular GP approximation methods, including Vecchia approximations [51] and Scaled Vecchia approximations (SVecchia) [27], both configured with a model condition size of 90 and a prediction condition size of 150, nearest neighbor GP (NNGP) [5, 11] with 30 neighbors, and local approximate GP (laGP) [15, 14] with 70 neighbors. We choose a larger conditioning size of Vecchia and SVecchia approaches and more neighbors in NNGP and laGP than the default setting, to improve the precision of the approximation methods, despite the increased computational cost, as shown in Table S4 and Fig. S5 in the Supplementary Material. All methods utilize the Matérn kernel with a roughness parameter of 2.5, except for laGP, which only allows the Gaussian kernel in the package.

5.2 Branin function

We first employ the Branin function to evaluate the performance of our IKF-CG algorithm in modeling incomplete lattice data [38]. The data are generated using

$$y(s_1, s_2) = \left(s_2 - \frac{5.1}{4\pi^2} s_1^2 + \frac{5}{\pi} s_1 - 6 \right)^2 + 10 \left(1 - \frac{1}{8\pi} \right) \cos(s_1) + 10 + \epsilon, \quad (28)$$

where ϵ is a Gaussian noise with the variance of $\sigma_0 = 10$. We consider a lattice with dimensions $n_1 = 100$ and $n_2 = 100$ over the domain $(s_{1,i}, s_{2,j}) \in [-5, 10] \times [0, 15]$ for $1 \leq i \leq n_1, 1 \leq j \leq n_2$. Three scenarios are analyzed, two having 20% missing locations at disks with different centers and one having 20% randomly selected missing locations. In each scenario, we repeat the simulation 20 times to account for variability from the noise. The observations from the first simulated case of a 20% disk missing scenario are shown in Fig. 9(a), with the underlying mean shown in panel (b). The prediction of the IKF-CG algorithm is plotted in panel (c), which demonstrates a high degree of accuracy.

Figure 10 presents violin plots of the NRMSE distribution for the missing regions in each scenario, comparing IKF-CG with the other four GP approximation methods, with dots indicating the average NRMSE across all experiments. The results reveal that all methods perform worse with disk-missing data compared to random-missing data, which is expected. Across all scenarios, IKF-CG consistently achieves the lowest NRMSE values. Specifically, the average NRMSE for IKF-CG is 0.022, 0.022, and 0.014 for scenarios shown in Fig. 10 (a)-(c) respectively, while the average NRMSE for other methods is at least twice as large. The average computation times for each scenario are provided in Table S4 in the Supplementary Material, showing that the order of the computational cost from all methods is similar. Overall, the IKF-CG method is more accurate than the alternatives for this example with a similar computational cost.

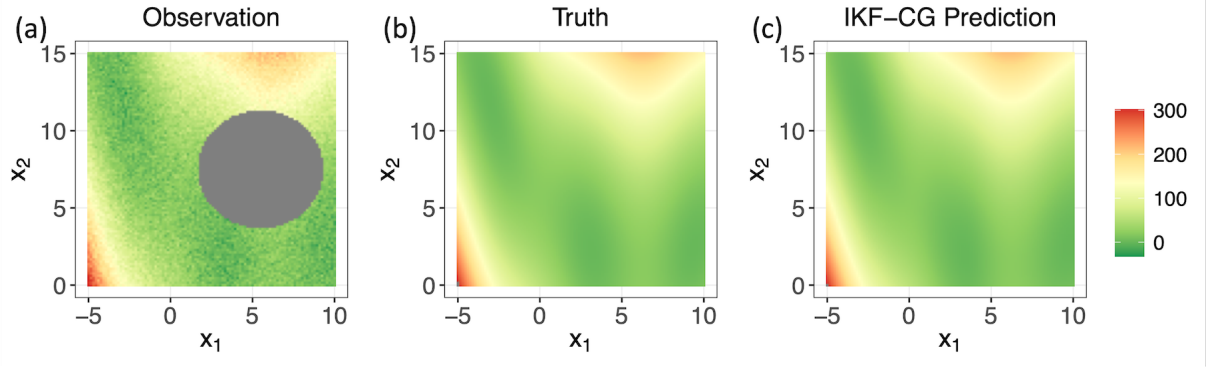


Figure 9: (a) Observed data from a simulation of the Branin function with the first disk missing. (b) Latent mean of the Branin function. (c) Predictions obtained using the IKF-CG algorithm.

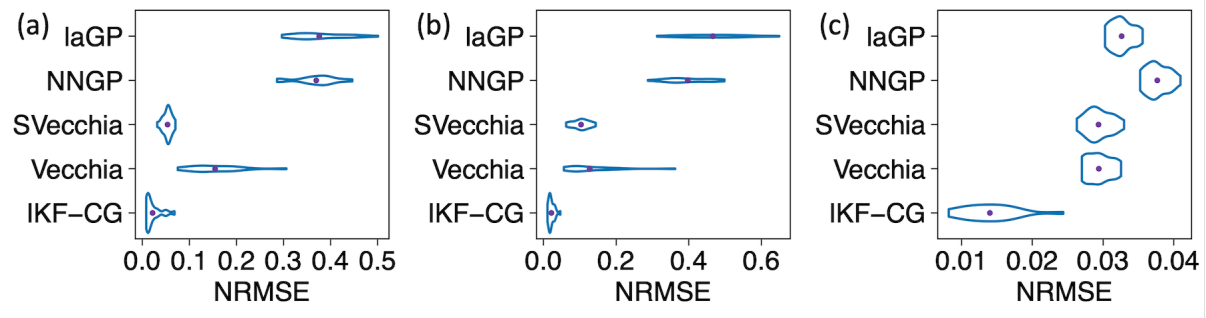


Figure 10: Violin plots illustrating the NRMSE of missing regions for different methods under 20% disk missing with the first center (panel (a)), 20% disk missing with the second center (panel (b)), and 20% random missing (panel (c)). The point on each violin represents the mean NRMSE for the respective methods.

5.3 Interferometric synthetic aperture radar interferogram

Interferometric synthetic aperture radar (InSAR) interferograms can measure ground deformation with centimeter-level precision, widely used for understanding geophysical processes and hazard quantification [2, 1]. We test our IKF-CG algorithm for predicting missing values in a COSMO-SkyMed satellite interferogram spanning from October 17, 2011, to May 4, 2012, for Kīlauea Volcano studied in [16]. The dataset is visualized in the Supplementary Material. For demonstration purposes, we investigate two types of missing data on a 200×200 lattice (disk missing and random missing) across five missing proportions (5%, 10%, 15%, 20%, and 25%).

Figures 11(a) and 11(b) illustrate the NRMSE for disk missing and random missing scenarios, respectively. The corresponding run times are provided in Fig. S5 the Supplementary Material, which shows the computational order of all approaches is similar. Generally, the predictive error is around an order of magnitude smaller for random missing data compared to disk missing data. In Fig. 11(a), IKF-CG outperforms other methods across most scenarios, especially at higher proportions of missing data (10%, 15%, 20%, and 25%), and it is also the fastest method for these higher proportions shown in Fig. S5 in the Supplementary Material. Figure 11(b) reveals that while Vecchia performs slightly better than the IKF-CG for the first four proportions in random missing scenarios, IKF-CG achieves the lowest NRMSE for the 25% missing scenario. The difference in NRMSE between these two methods is small. Though predicting missing values in lattice data is

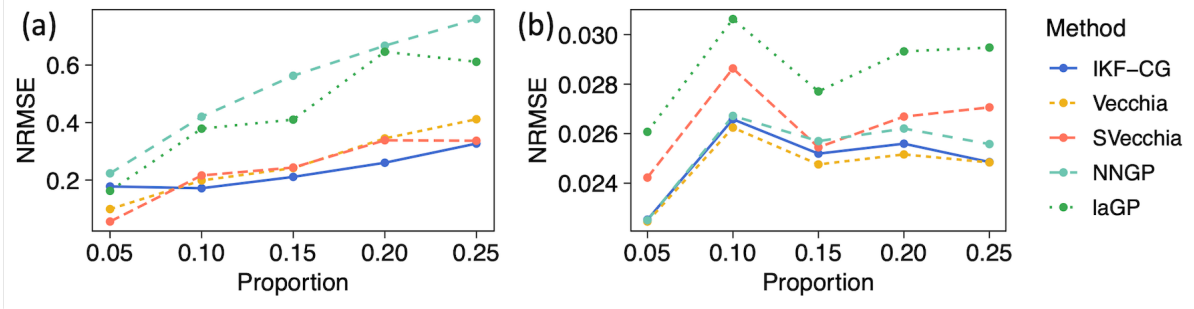


Figure 11: The NRMSE of the missing regions in disk missing (panel (a)) and random missing (panel (b)) scenarios for interferograms.

not the main motivating application in our study, the results underscore the accuracy and scalability of the IKF-CG algorithm in different applications.

6 Concluding remarks

We outline a few new avenues for future research. While the ensemble Kalman filter [9, 48] and particle filter [28, 10] are commonly used for filtering and smoothing in nonlinear or non-Gaussian dynamical systems, these methods typically assume that the forward equations of the dynamics are known. It may be of interest to integrate the new approach in estimating latent interaction functions when forward equations are unavailable or computationally intensive. Additionally, the proposed inverse Kalman filter approach may be used as a fast alternative for constructing latent factor models of multivariate time series [29], autoregressive-exogenous models [39] and generalized factor processes for categorical observations [7]. Finally, the new approach, along with the CG method, may motivate new approximation approaches for GPs with multi-dimensional input spaces.

Acknowledgement

Xinyi Fang acknowledges partial support from the BioPACIFIC Materials Innovation Platform of the National Science Foundation under Award No. DMR-1933487.

Supplementary Material

The Supplementary Material contains (i) a summary of the connection between the Gaussian Processes with Matérn covariance functions with roughness parameters being 0.5 and 2.5 and dynamic linear models, along with the closed-form of matrices $\mathbf{F}_{t,j}$, $\mathbf{G}_{t,j}$ and $\mathbf{W}_{t,j}$; (ii) the conjugate gradient algorithm; (iii) detailed procedures for the scalable computation of the predictive distribution in particle dynamics; (iv) the derivation of computational complexity in parameter estimation; and (v) additional numerical results.

Appendix A. Kalman Filter

The Kalman filter [24] for dynamic linear models in (1)-(2) is summarized in Lemma 5.

Lemma 5 (Kalman Filter). *Let $\boldsymbol{\theta}_{t-1} \mid \mathbf{y}_{1:t-1} \sim \mathcal{MN}(\mathbf{m}_{t-1}, \mathbf{C}_{t-1})$. Recursively for $t = 2, \dots, N$:*

(i) The one-step-ahead predictive distribution of $\boldsymbol{\theta}_t$ given $\mathbf{y}_{1:t-1}$ is

$$\boldsymbol{\theta}_t \mid \mathbf{z}_{1:t-1} \sim \mathcal{MN}(\mathbf{b}_t, \mathbf{B}_t), \quad (29)$$

with $\mathbf{b}_t = \mathbf{G}_t \mathbf{m}_{t-1}$ and $\mathbf{B}_t = \mathbf{G}_t \mathbf{C}_{t-1} \mathbf{G}_t^T + \mathbf{W}_t$.

(ii) The one-step-ahead predictive distribution of y_t given $\mathbf{y}_{1:t-1}$ is

$$y_t \mid \mathbf{y}_{1:t-1} \sim \mathcal{N}(f_t, Q_t), \quad (30)$$

with $f_t = \mathbf{F}_t \mathbf{b}_t$, and $Q_t = \mathbf{F}_t \mathbf{B}_t \mathbf{F}_t^T + V_t$.

(iii) The filtering distribution of $\boldsymbol{\theta}_t$ given $\mathbf{y}_{1:t}$ follows

$$\boldsymbol{\theta}_t \mid \mathbf{y}_{1:t} \sim \mathcal{MN}(\mathbf{m}_t, \mathbf{C}_t), \quad (31)$$

with $\mathbf{m}_t = \mathbf{b}_t + \mathbf{B}_t \mathbf{F}_t^T Q_t^{-1} (y_t - f_t)$ and $\mathbf{C}_t = \mathbf{B}_t - \mathbf{B}_t \mathbf{F}_t^T Q_t^{-1} \mathbf{F}_t \mathbf{B}_t$.

Lemma 6. Denote $\tilde{\mathbf{y}} = (\tilde{y}_1, \dots, \tilde{y}_N)^T = \mathbf{L}^{-1} \mathbf{y}$, where \mathbf{L} is the factor in Cholesky decomposition of a positive definite covariance $\boldsymbol{\Sigma}$, with $\boldsymbol{\Sigma} = \text{cov}[\mathbf{y}]$ and $\mathbf{y} = (y_1, \dots, y_N)^T$ defined as in (1). We have

$$\tilde{y}_t = \frac{y_t - f_t}{Q_t^{1/2}}, \quad (32)$$

where f_t and Q_t are defined in Eq. (30). Furthermore, the t th diagonal term of \mathbf{L} is $L_{t,t} = Q_t^{1/2}$.

Proof. From Eq. (30) in step (ii) of the Kalman filter in Lemma 5, we have

$$p(\mathbf{y}_{1:N}) = \prod_{t=1}^N \left\{ (2\pi Q_t)^{-1/2} \exp\left(-\frac{(y_t - f_t)^2}{2Q_t}\right) \right\}. \quad (33)$$

Additionally, since \mathbf{y} follows a zero-mean multivariate normal distribution, we have

$$p(\mathbf{y}_{1:N}) = (2\pi)^{-N/2} |\boldsymbol{\Sigma}|^{-1/2} \exp\left(-\frac{1}{2} (\mathbf{L}^{-1} \mathbf{y})^T (\mathbf{L}^{-1} \mathbf{y})\right), \quad (34)$$

where \mathbf{L} is the Cholesky factor of $\boldsymbol{\Sigma}$, a lower triangular matrix with positive diagonal entries. By equating Eqs. (33) and (34), we have

$$\sum_{t=1}^N \frac{(y_t - f_t)^2}{Q_t} = (\mathbf{L}^{-1} \mathbf{y})^T (\mathbf{L}^{-1} \mathbf{y}) = \sum_{t=1}^N \tilde{y}_t^2, \quad (35)$$

$$\prod_{t=1}^N Q_t^{1/2} = |\boldsymbol{\Sigma}|^{1/2} = |\mathbf{L}| = \prod_{t=1}^N L_{t,t}. \quad (36)$$

Since the Kalman filter operates incrementally and applies to any number of observations, these equalities hold not only for the entire set of observations up to N but also for any subset up to $t' \leq N$. This means the expressions in Eqs. (35) and (36) are valid for sums and products up to any $t' = 1, \dots, N$. We will use this property to prove both statements of the lemma by mathematical induction.

First, we prove $\tilde{y}_t = (y_t - f_t)/Q_t^{1/2}$ for $t = 1, \dots, N$. When we consider only the first observation, i.e., $t' = 1$, the matrix $\boldsymbol{\Sigma}$ reduces to the scalar Q_1 , and the statement directly follows from the

definition of the Cholesky decomposition which has positive diagonals and $f_1 = 0$. For the first $t' - 1$ observations, we have $\sum_{t=1}^{t'-1} (y_t - f_t)^2 / Q_t = \sum_{t=1}^{t'-1} \tilde{y}_t^2$. Including the t' th observation, we get $\sum_{t=1}^{t'} (y_t - f_t)^2 / Q_t = \sum_{t=1}^{t'} \tilde{y}_t^2$. Subtracting the sum of the first $t' - 1$ observations, we have $(y_{t'} - f_{t'})^2 / Q_{t'} = \tilde{y}_{t'}^2$, which gives

$$\tilde{y}_{t'} = \frac{y_{t'} - f_{t'}}{Q_{t'}^{1/2}} \quad \text{or} \quad \tilde{y}_{t'} = -\frac{y_{t'} - f_{t'}}{Q_{t'}^{1/2}}. \quad (37)$$

Let $\tilde{L}_{t',t}$ denote the (t', t) th element of \mathbf{L}^{-1} . We can write

$$\tilde{y}_{t'} = \sum_{t=1}^{t'} \tilde{L}_{t',t} y_t. \quad (38)$$

By equating the coefficient of $y_{t'}$ in Eqs. (37) and (38), we obtain $\tilde{L}_{t',t'} = Q_t^{1/2}$ or $\tilde{L}_{t',t'} = -Q_t^{1/2}$. However, since $\mathbf{\Sigma} = \mathbf{L}\mathbf{L}^T$, we have $\mathbf{\Sigma}^{-1} = (\mathbf{L}^{-1})^T \mathbf{L}^{-1}$, indicating \mathbf{L}^{-1} is the upper-triangular Cholesky factor of a positive definite matrix $\mathbf{\Sigma}^{-1}$. Thus, the diagonal entry $\tilde{L}_{t',t'}$ of $\mathbf{\Sigma}^{-1}$ must be positive, and the only solution is $\tilde{y}_{t'} = (y_{t'} - f_{t'}) / Q_{t'}^{1/2}$.

The second statement, $L_{t,t} = Q_t^{1/2}$, follows using similar logic with Eq. (36) by mathematical induction. The detailed proof is omitted here for brevity. \square

Appendix B. Proofs for Section 2

In the following proofs, we first prove Lemma 2, as this lemma is essential for proving Lemma 3. The outcome of Lemma 3 is then used to prove Lemma 1. The proof of lemma 4 is presented at the end.

of Lemma 2. For any $t = 1, \dots, N$, we invert Eq. (32) in Kalman filter to compute $x_t = f_t + Q_t^{1/2} \tilde{x}_t$ with $f_t = \mathbf{F}_t \mathbf{b}_t$. The other two steps are from the Kalman filter with a known observation x_t . By Lemma 6, for any N-vector \mathbf{x} , the second step of Kalman filter produces $\tilde{\mathbf{x}} = \mathbf{L}^{-1} \mathbf{x}$. As the steps of Kalman filter are reversed in Lemma 2, we have $\mathbf{x} = \mathbf{L} \tilde{\mathbf{x}}$ for any N-vector $\tilde{\mathbf{x}}$. \square

of Lemma 3. Denote $\mathbf{x} = \mathbf{L} \tilde{\mathbf{x}}$. The t' th entry $x_{t'}$ is

$$x_{t'} = \sum_{t=1}^{t'} L_{t',t} \tilde{x}_t. \quad (39)$$

We will prove this by mathematical induction. When $t' = 1$, $L_{1,1} = Q_1^{1/2}$ by Lemma 6. For any $t' - 1 > t$ assume $L_{t'-1,t} = Q_t^{1/2} \ell_{t'-1,t} = Q_t^{1/2} \mathbf{F}_{t'-1} (\prod_{l=t+1}^{t'-1} \mathbf{G}_l) \mathbf{K}_t$. From Eq. (39), for $t' > t + 1$ we have

$$x_{t'-1} = \mathbf{F}_{t'-1} \left(Q_t^{\frac{1}{2}} \left(\prod_{l=t+1}^{t'-1} \mathbf{G}_l \right) \mathbf{K}_t \tilde{x}_t + \mathbf{c}_{t'-1,t} \right) + Q_{t'-1}^{\frac{1}{2}} \tilde{x}_{t'-1}, \quad (40)$$

where $\mathbf{c}_{t'-1,t}$ is a q vector that does not depend on \tilde{x}_t and $\tilde{x}_{t'-1}$. Comparing with Eq. (7) in Lemma

2, we have $\mathbf{b}_{t'-1} = Q_t^{1/2}(\prod_{l=t+1}^{t'-1} \mathbf{G}_l \mathbf{K}_t x_t + \mathbf{c}_{t'-1,t})$. Iterate through equations in Lemma 2, we have

$$\begin{aligned} \mathbf{m}_{t'-1} &= Q_t^{\frac{1}{2}} \left(\prod_{l=t+1}^{t'-1} \mathbf{G}_l \right) \mathbf{K}_t \tilde{x}_t + \mathbf{c}_{t'-1,t} + \mathbf{K}_{t'-1} Q_{t'-1}^{\frac{1}{2}} \tilde{x}_{t'-1}, \\ \mathbf{b}_{t'} &= Q_t^{\frac{1}{2}} \left(\prod_{l=t+1}^{t'} \mathbf{G}_l \right) \mathbf{K}_t \tilde{x}_t + \mathbf{G}_{t'} \left(\mathbf{c}_{t'-1,t} + \mathbf{K}_{t'-1} Q_{t'-1}^{\frac{1}{2}} \tilde{x}_{t'-1} \right), \\ x_{t'} &= \mathbf{F}_{t'} \left(Q_t^{1/2} \left(\prod_{l=t+1}^{t'} \mathbf{G}_l \right) \mathbf{K}_t \tilde{x}_t + \mathbf{c}_{t',t} \right) + Q_{t'}^{\frac{1}{2}} \tilde{x}_{t'}, \end{aligned} \quad (41)$$

where $\mathbf{c}_{t',t} = \mathbf{G}_{t'}(\mathbf{c}_{t'-1,t} + \mathbf{K}_{t'-1} Q_{t'-1}^{1/2} \tilde{x}_{t'-1})$, independent of \tilde{x}_t . By Eqs. (39) and (41), we have $L_{t',t} = Q_t^{1/2} \mathbf{F}_{t'} (\prod_{l=t+1}^{t'} \mathbf{G}_l) \mathbf{K}_t = Q_t^{1/2} \ell_{t',t}$ for $t' > t + 1$.

For $t' = t + 1$, we have $L_{t',t} = Q_{t'-1}^{1/2}$ by Lemma 6. Iterate through equations in Lemma 2, we also have

$$x_{t'} = \mathbf{F}_{t'} \mathbf{G}_{t'} (\mathbf{b}_{t'-1} + \mathbf{K}_{t'-1} Q_{t'-1}^{\frac{1}{2}} \tilde{x}_{t'-1}) + Q_{t'}^{\frac{1}{2}} \tilde{x}_{t'}. \quad (42)$$

By equating (39) and (42), we have $L_{t',t'-1} = Q_{t'-1}^{1/2} \mathbf{F}_{t'} \mathbf{G}_{t'} \mathbf{K}_{t'-1} = Q_{t'-1}^{1/2} \ell_{t',t'-1}$.

When $t' = t$, Lemma 6 gives $L_{t',t} = Q_t^{1/2}$. The results hold for any $t' \geq t$, thus concluding the proof. \square

of Lemma 1. Denote $\tilde{\mathbf{x}} = \mathbf{L}^T \mathbf{u}$. The N th and $(N - 1)$ th entries of $\tilde{\mathbf{x}}$ directly follow from Lemma 3. For $t = N - 2, \dots, 1$, we will prove by induction. For the t th entry x_t , by Lemma 3, we have

$$\tilde{x}_t = \sum_{t'=t}^N L_{t',t} u_{t'} = Q_t^{\frac{1}{2}} \left(\sum_{t'=t+2}^N \ell_{t',t} u_{t'} + \ell_{t+1,t} u_{t+1} + u_t \right). \quad (43)$$

Thus, it suffices to prove $\tilde{\ell}_{t+1,t} = \mathbf{g}_{t+1} \mathbf{G}_{t+1} \mathbf{K}_t = \sum_{t'=t+2}^N \ell_{t',t} u_{t'}$. When $t = N - 2$,

$$\ell_{N,N-2} u_N = \mathbf{F}_N \mathbf{G}_N \mathbf{G}_{N-1} \mathbf{K}_{N-2} u_N = \mathbf{g}_{N-1} \mathbf{G}_{N-1} \mathbf{K}_{N-2} = \tilde{\ell}_{N-1,N-2}.$$

Then assume for any $t \leq N - 2$, $\mathbf{g}_{t+1} \mathbf{G}_{t+1} \mathbf{K}_t = \sum_{t'=t+2}^N \ell_{t',t} u_{t'}$. From Lemma 3, we have

$$\sum_{t'=t+2}^N \ell_{t',t} u_{t'} = \sum_{t'=t+2}^N \mathbf{F}_{t'} \left(\prod_{l=t+1}^{t'} \mathbf{G}_l \right) \mathbf{K}_t u_{t'} = \left\{ \sum_{t'=t+2}^N \mathbf{F}_{t'} \left(\prod_{l=t+2}^{t'} \mathbf{G}_l \right) u_{t'} \right\} \mathbf{G}_{t+1} \mathbf{K}_t.$$

Then

$$\mathbf{g}_{t+1} = \sum_{t'=t+2}^N \mathbf{F}_{t'} \left(\prod_{l=t+2}^{t'} \mathbf{G}_l \right) u_{t'}.$$

Similarly for $(t - 1)$ th entry,

$$\begin{aligned} \sum_{t'=t+1}^N \ell_{t',t-1} u_{t'} &= \left\{ \sum_{t'=t+1}^N \mathbf{F}_{t'} \left(\prod_{l=t+1}^{t'} \mathbf{G}_l \right) u_{t'} \right\} \mathbf{G}_t \mathbf{K}_{t-1} \\ &= \{ \mathbf{g}_{t+1} \mathbf{G}_{t+1} + \mathbf{F}_{t+1} \mathbf{G}_{t+1} u_{t+1} \} \mathbf{G}_t \mathbf{K}_{t-1}. \end{aligned}$$

We have $\mathbf{g}_t \mathbf{G}_t \mathbf{K}_{t-1} = \sum_{t'=t+1}^N \ell_{t',t-1} u_{t'}$. \square

of Lemma 4. In Lemma 1, the iterative algorithm gives $\tilde{\mathbf{x}} = \mathbf{L}^T \mathbf{u}$ for any N-vector \mathbf{u} . We invert Eq. (3) to get $u_t = Q_t^{-1/2} \tilde{x}_t - \tilde{\ell}_{t+1,t} - \ell_{t+1,t} u_{t+1}$ for any t . Since we reverse the steps of the iterative algorithm in Lemma 1, we have $\mathbf{u} = (\mathbf{L}^T)^{-1} \tilde{\mathbf{x}}$ for any N-vector $\tilde{\mathbf{x}}$. \square

Appendix C. Scalable computation of the predictive distribution in learning particle interactions

This section outlines the procedure to calculate the predictive mean and variance in (15) using the IKF-CG algorithm for learning particle interactions. More detailed computations are summarized in the Supplementary Material.

First, to compute the predictive mean for a single input d^* , the primary computational task is solving for $\hat{\mathbf{u}} = \Sigma_y^{-1} \mathbf{y}$, where \mathbf{y} is a vector of \tilde{N} dimensions. This is equivalent to solving the linear system $\Sigma_y \hat{\mathbf{u}} = \mathbf{y}$, which can be iteratively computed by the CG algorithm. Starting with an initial guess $\mathbf{u}_{(0)} = \mathbf{0}$, the CG method iteratively refines the solution $\mathbf{u}_{(k)}$ within the Krylov subspace $\text{span}[\mathbf{y}, \Sigma_y \mathbf{y}, \dots, \Sigma_y^{k-1} \mathbf{y}]$ at each step k , minimizing the norm $\|\hat{\mathbf{u}} - \mathbf{u}_{(k)}\|_{\Sigma_y}^2 = (\hat{\mathbf{u}} - \mathbf{u}_{(k)})^T \Sigma_y (\hat{\mathbf{u}} - \mathbf{u}_{(k)})$. The IKF algorithm, combined with the sparsity of \mathbf{A}_j , significantly enhances the efficiency of the most demanding computation of $\Sigma_y \mathbf{u}$. While the IKF algorithm is applied to ordered inputs \mathbf{d}_j , the original order must be reinstated for subsequent calculations.

Second, for computing the predictive mean of the interaction function over N_j^* inputs $\mathbf{d}_j^* = [d_{1,j}^*, \dots, d_{N_j^*,j}^*]^T$, which may be unordered, we proceed as follows. After obtaining $\hat{\mathbf{u}}_j = \mathbf{A}_j^T \Sigma_y^{-1} \mathbf{y}$, direct calculation of the posterior mean, which involves matrix-vector multiplication $\Sigma_j^{(u)} (\mathbf{d}_j^*)^T \hat{\mathbf{u}}_j$ that costs $\mathcal{O}(N_j^* N_j)$, remains intensive for large N_j^* , especially in parameter estimation requiring multiple iterations. To reduce computational complexity, we generate an augmented vector $\mathbf{d}_j^{\text{aug},(u)} = [(\mathbf{d}_j^*)^T, (\mathbf{d}_j^{(u)})^T]^T$ and the augmented $(N_j^* + N_j)$ -vector $\hat{\mathbf{u}}_j^{\text{aug},(u)} = [\mathbf{0}_{N_j^*}^T, \hat{\mathbf{u}}_j^T]^T$. The predictive mean $\Sigma_j^{(u)} (\mathbf{d}_j^*)^T \hat{\mathbf{u}}_j$ is obtained by extracting the first N_j^* terms in $\Sigma_j^{\text{aug},(u)} \hat{\mathbf{u}}_j^{\text{aug},(u)}$, where $\Sigma_j^{\text{aug},(u)}$ is the covariance matrix of $\mathbf{d}_j^{\text{aug},(u)}$, and this product can be efficiently computed using the IKF algorithm. This approach reduces computational operations and storage cost to $\mathcal{O}(q_j^3 (N_j^* + N_j))$ without approximation.

Third, for the predictive variance for a single input d^* , the IKF algorithm is again used to expedite the computation of the term $\Sigma_y^{-1} \mathbf{A}_j \Sigma_j^{(u)} (d^*)$. Unlike the posterior mean computation, which is required multiple times in parameter estimation, the calculation of the posterior variance only needs to be performed once, making the computation typically feasible after being accelerated by the IKF algorithm.

Appendix D. Parameter estimation

The parameters in the model include the range parameters $\gamma = (\gamma_1, \dots, \gamma_J)$, the variance of each latent factor process $\sigma^2 = (\sigma_1^2, \dots, \sigma_J^2)$, the variance of the noise σ_0^2 , and other physical parameters \mathbf{r} , such as the radius of interactions between particles. For computational efficiency, we define $\boldsymbol{\eta} = (\eta_1, \dots, \eta_J)$ with $\eta_j^2 = \sigma_j^2 / \sigma_0^2$ for $j = 1, \dots, J$ as the ratio of the variance of the J interaction functions to the variance of the noise, and σ_0^2 can be marginalized out explicitly. This parameterization is preferred over σ_0^2 / σ_j^2 , because σ_j^2 could be close to zero if the effect of the j th particle interaction is small, thus causing numerical instability. In contrast, the variance

σ_0^2 , accounting for measurement noise and model inadequacy, is typically larger than zero, making the parameterization by $\boldsymbol{\eta}$ a preferred choice for our applications. In a previous study [18], the fast algorithm is only applicable for a GP with an exponential kernel with fixed hyperparameters of covariance functions and physical parameters. This study employs two methods for estimating these parameters applicable for GPs with any DLM induced covariances, and utilizes the residual bootstrap method for uncertainty quantification. All these approaches can be accelerated using the proposed IKF algorithm.

First, we focus on the cross-validation approach for parameters estimation, where we split the observations into training and hold-out validation sets, denoted as \mathbf{y}_{train} and \mathbf{y}_{val} for N_{train} training and N_{val} validation vectors, respectively. Parameters are estimated by minimizing a loss function, chosen as the mean squared error, during cross-validation:

$$(\hat{\boldsymbol{\eta}}, \hat{\boldsymbol{\gamma}}, \hat{\mathbf{r}}) = \operatorname{argmax}_{(\boldsymbol{\eta}, \boldsymbol{\gamma}, \mathbf{r})} \left\{ \frac{1}{N_{val}} (\hat{\mathbf{y}}_{val} - \mathbf{y}_{val})^T (\hat{\mathbf{y}}_{val} - \mathbf{y}_{val}) \right\}, \quad (44)$$

where for application in Section 3.1, $\hat{\mathbf{y}}_{val} = \sum_{j=1}^J \mathbf{A}_{j,val} \hat{\mathbf{z}}_{j,val}$, with $\hat{\mathbf{z}}_{j,val}$ being the posterior mean of the latent interaction function for cross-validation inputs \mathbf{d}_j^* of size N_j^* and $\mathbf{A}_{j,val}$ being a sparse latent factor loading matrix of dimensions $N_{val} \times N_j^*$, for $j = 1, \dots, J$. For application in Section 3.2, $\hat{\mathbf{y}}_{val} = \mathbf{A}_{val} \hat{\mathbf{z}}_v$, where \mathbf{A}_{val} is the identity matrix with rows corresponding to non-validation entries removed and is of dimension $N_{val} \times N$.

Conditioning on other estimated parameters, the maximum likelihood estimate of σ_0^2 is obtained via $\hat{\sigma}_0^2 = \mathbf{y}^T \mathbf{R}_y^{-1} \mathbf{y} / \tilde{N}$, where $\mathbf{R}_y = \boldsymbol{\Sigma}_y / \sigma_0^2$. The computation of $\mathbf{R}_y^{-1} \mathbf{y}$ can be efficiently handled using the IKF-CG algorithm. The parameters are then transformed to obtain $\hat{\sigma}_j^2 = \hat{\eta}_j \hat{\sigma}_0^2$ and $\hat{\sigma}^2 = \hat{\eta} \hat{\sigma}_0^2$ in applications of Sections 3.1 and 3.2, respectively.

Next, we discuss the maximum likelihood estimation, which requires computing the determinant of a large $\tilde{N} \times \tilde{N}$ matrix $\boldsymbol{\Sigma}_y$. This computationally infeasible step, requiring $\mathcal{O}(\tilde{N}^3)$ computation, can be addressed with a low-rank approximation $\boldsymbol{\Sigma}_a$ of the matrix $\boldsymbol{\Sigma}_0$ [43], with $\boldsymbol{\Sigma}_0 = \sum_{j=1}^J \mathbf{A}_j \boldsymbol{\Sigma}_j^{(u)} \mathbf{A}_j^T / \sigma_0^2$ and $\boldsymbol{\Sigma}_0 = \mathbf{A} \boldsymbol{\Sigma} \mathbf{A}^T / \sigma_0^2$ for applications in Sections 3.1 and 3.2, respectively. This approach approximates the log-determinant of the covariance matrix by $\log |\boldsymbol{\Sigma}_a + \mathbf{I}_{\tilde{N}}| \approx \log |\boldsymbol{\Sigma}_0 + \mathbf{I}_{\tilde{N}}|$. The key assumption is that the matrix $\boldsymbol{\Sigma}_0$ has N_0 dominant eigenvalues, a valid assumption for both applications.

To construct $\boldsymbol{\Sigma}_a$, we first set the dimension N_0 of the matrix $\boldsymbol{\Sigma}_a$ with $N_0 \ll \tilde{N}$ and initialize a $\tilde{N} \times N_0$ matrix $\boldsymbol{\Omega}$ with i.i.d. standard normal entries. Next, we compute $\boldsymbol{\Sigma}_0^{M_0} \boldsymbol{\Omega}$, where M_0 is a positive integer. The QR decomposition of $\boldsymbol{\Sigma}_0^{M_0} \boldsymbol{\Omega}$ yields an orthogonal matrix \mathbf{U} , and the low-rank matrix $\boldsymbol{\Sigma}_a$ is defined as $\boldsymbol{\Sigma}_a = \mathbf{U}^T \boldsymbol{\Sigma}_0 \mathbf{U}$. All computations can be accelerated using the IKF method, resulting in a cost of $\mathcal{O}(M_0 \sum_{j=1}^J N_j (\log(N_j) + D_y + q_j^3))$ and $\mathcal{O}(q^3 M_0 N)$ for applications in Sections 3.1 and 3.2, respectively. When the gap between dominant and sub-dominant eigenvalues is large, a small M_0 suffices. Then with the maximum likelihood estimate of $\hat{\sigma}_0^2 = \mathbf{y}^T \mathbf{R}_y^{-1} \mathbf{y} / \tilde{N}$, parameters $(\boldsymbol{\eta}, \boldsymbol{\gamma}, \mathbf{r})$ are estimated by maximizing the logarithm of the marginal likelihood after integrating out the latent factors:

$$(\hat{\boldsymbol{\eta}}, \hat{\boldsymbol{\gamma}}, \hat{\mathbf{r}}) = \operatorname{argmax}_{(\boldsymbol{\eta}, \boldsymbol{\gamma}, \mathbf{r})} \left\{ -\frac{1}{2} \log |\boldsymbol{\Sigma}_a + \mathbf{I}_{N_0}| - \frac{\tilde{N}}{2} \log (\mathbf{y}^T \mathbf{R}_y^{-1} \mathbf{y}) \right\}. \quad (45)$$

This approximation is as fast as cross-validation, with small approximation errors in our applications, as demonstrated in Fig. 3(c) for a simulated study.

Lastly, we employ residual bootstrap to quantify uncertainty in parameter estimation [6, 44]. This involves computing the posterior mean of the observations $\hat{\mathbf{y}}$ using the predictive interaction

Steps	IKF-CG	CG	Direct computation
Form covariance	/	$\mathcal{O}(M \sum_{j=1}^J N_j^2)$	$\mathcal{O}(M \sum_{j=1}^J N_j^2)$
Sort inputs	$\mathcal{O}(M \sum_{j=1}^J (N_j^{all}) \log(N_j^{all}))$	/	/
Compute weights	$\mathcal{O}(MS \sum_{j=1}^J (D_y + q_j^3) N_j)$	$\mathcal{O}(MS \sum_{j=1}^J N_j^2)$	$\mathcal{O}(M \tilde{N}^3)$
Compute loss	$\mathcal{O}(M \sum_{j=1}^J (N_j^{all}))$	$\mathcal{O}(M \sum_{j=1}^J N_j^* N_j)$	$\mathcal{O}(M \sum_{j=1}^J N_j^* N_j)$

Table 3: The computational complexity of parameter estimation with M iterations of numerical optimization of the parameters in learning particle interactions with $N_j^{all} = N_j + N_j^*$. The CG and direct computation algorithms involve forming an $N_j \times N_j$ covariance matrix, while the IKF-CG only requires computing ordered inputs. We assume computing weights $\hat{\mathbf{u}}_j = \mathbf{A}_j^T \Sigma_y^{-1} \mathbf{y}$ is a separate step with complexity shown in the third row of the table.

function with estimated parameters $(\hat{\boldsymbol{\eta}}, \hat{\boldsymbol{\gamma}}, \hat{\mathbf{r}})$, and calculating residuals $\mathbf{e} = \mathbf{y} - \hat{\mathbf{y}} = [e_1, \dots, e_N]^T$. We then generate a new set of \tilde{N} residuals $\mathbf{e}^* = [e_1^*, \dots, e_{\tilde{N}}^*]^T$, such that $\text{pr}(e_i^* = e_{i'}) = 1/\tilde{N}$ for $i' = 1, \dots, \tilde{N}$. This creates a new set of bootstrap observations via $\mathbf{y}^* = \hat{\mathbf{y}} + \mathbf{e}^*$. Using the same inputs and bootstrap observations, we refit the model to obtain the estimates $\hat{\boldsymbol{\gamma}}^*$, $\hat{\boldsymbol{\eta}}^*$, and $\hat{\mathbf{r}}^*$. Repeating this procedure B times, we obtain confidence intervals by taking the percentiles of these B estimates for each parameter.

Appendix E. Computational complexity

The primary computational challenge lies in estimating the hyperparameters in the model. Here, we mainly focus on parameter estimation with cross-validation. The computational cost of maximum likelihood estimation is similar. First, we analyze the computational complexity of learning particle interactions in Section 3.1. Table 3 lists the computational complexity of three different parameter estimation algorithms, namely our IKF-CG method, the conventional CG algorithm, and direct computation via Cholesky decomposition and forward-backward solver (see Appendix A.4 of [42]). We assume that all algorithms require M iterations for parameter estimation, and in each iteration, the CG and IKF-CG methods require S iterations to compute $\Sigma_y^{-1} \mathbf{y}$. In our applications, both M and S are around a hundred to ensure the approximation error is a few orders of magnitude smaller than the predictive error (Fig. 3). We will pre-process the particle information and save the results in coarse-grained grids, shown in Fig. S1 in Supplementary Material, which only takes $\mathcal{O}(\tilde{N})$ operations. The derivation and computational complexity of this step, along with all steps shown in Table 3, are summarized in the Supplementary Material.

In Table 3, \tilde{N} and N_j stand for the number of observations and the number of inputs in the j th interaction, respectively, which are typically large in real-world applications, ranging from 10^3 to 10^6 . The number of validation inputs N_j^* for the j th interaction has the same order as N_j , and all other quantities listed are relatively small. The number of interactions, J , is typically 1 or 2. For modeling interaction functions, Matérn covariances with roughness parameters 0.5 and 2.5 are used, corresponding to $q_j = 1$ and $q_j = 3$, respectively. The dimension of the output vector, D_y , is generally no more than 3 in practical scenarios. Moreover, the average number of neighbors p_j in the j th interaction is typically much smaller than the number of particles, not exceeding 10 in our applications.

The direct computation method requires $\mathcal{O}(M \sum_{j=1}^J N_j^2)$ and $\mathcal{O}(M \tilde{N}^3)$ operations for forming the covariance matrix and computing its inversion, respectively, which is prohibitively slow for large dataset. The CG algorithm is typically faster than the direct computation method, but still

prohibitively expensive to compute $\hat{\mathbf{u}}_j = \mathbf{A}_j^T \boldsymbol{\Sigma}_y^{-1} \mathbf{y}$ with MS iterations for parameter estimation. The IKF-CG algorithm significantly improves the computational order by removing the cost of forming the $N_j \times N_j$ covariance matrix and computing the weights and loss. It is approximately N_j times faster than the CG algorithm for matrix-vector multiplications involving a dense covariance $\boldsymbol{\Sigma}_j$. The scalability of the IKF-CG algorithm makes it a suitable alternative for fast parameter estimation and predictions.

The computational cost associated with modeling incomplete lattice data using the IKF-CG algorithm is more straightforward. Specifically, parameter estimation for IKF-CG by cross validation which primarily involves computing the predictive mean in Eq. (19), requires $\mathcal{O}(MSq^3N)$ operations. This cost of the IKF-CG algorithm is significantly lower than that of direct computation methods, which require $\mathcal{O}(MN^2)$ for forming the covariance matrix and $\mathcal{O}(M\tilde{N}^3)$ for matrix inversion.

References

- [1] Kyle R Anderson, Ingrid A Johanson, Matthew R Patrick, Mengyang Gu, Paul Segall, Michael P Poland, Emily K Montgomery-Brown, and Asta Miklius. Magma reservoir failure and the onset of caldera collapse at Kilauea volcano in 2018. *Science*, 366(6470), 2019.
- [2] Roland Bürgmann, Paul A Rosen, and Eric J Fielding. Synthetic Aperture Radar Interferometry to Measure Earth’s Surface Topography and Its Deformation. *Annual Review of Earth and Planetary Sciences*, 28(1):169–209, may 2000.
- [3] Hugues Chaté, Francesco Ginelli, Guillaume Grégoire, Fernando Peruani, and Franck Raynaud. Modeling collective motion: variations on the Vicsek model. *The European Physical Journal B*, 64(3):451–456, 2008.
- [4] Noel Cressie and Gardar Johannesson. Fixed rank kriging for very large spatial data sets. *Journal of the Royal Statistical Society: Series B (Statistical Methodology)*, 70(1):209–226, 2008.
- [5] Abhirup Datta, Sudipto Banerjee, Andrew O Finley, and Alan E Gelfand. Hierarchical nearest-neighbor Gaussian process models for large geostatistical datasets. *Journal of the American Statistical Association*, 111(514):800–812, 2016.
- [6] Anthony Christopher Davison and David Victor Hinkley. *Bootstrap methods and their application*. Number 1. Cambridge university press, 1997.
- [7] Daniele Durante and David B Dunson. Nonparametric Bayes dynamic modelling of relational data. *Biometrika*, 101(4):883–898, 2014.
- [8] James Durbin and Siem Jan Koopman. *Time series analysis by state space methods*, volume 38. OUP Oxford, 2012.
- [9] Geir Evensen. *Data assimilation: the ensemble Kalman filter*. Springer Science & Business Media, 2009.
- [10] Paul Fearnhead, David Wyncoll, and Jonathan Tawn. A sequential smoothing algorithm with linear computational cost. *Biometrika*, 97(2):447–464, 2010.

- [11] Andrew O. Finley, Abhirup Datta, and Sudipto Banerjee. spNNGP R Package for Nearest Neighbor Gaussian Process Models. *Journal of Statistical Software*, 103(5):1–40, 2022.
- [12] Reinhard Furrer, Marc G Genton, and Douglas Nychka. Covariance tapering for interpolation of large spatial datasets. *Journal of Computational and Graphical Statistics*, 15(3):502–523, 2006.
- [13] Francesco Ginelli, Fernando Peruani, Markus Bär, and Hugues Chaté. Large-scale collective properties of self-propelled rods. *Physical review letters*, 104(18):184502, 2010.
- [14] Robert B Gramacy. lagp: large-scale spatial modeling via local approximate Gaussian processes in R. *Journal of Statistical Software*, 72(1):1–46, 2016.
- [15] Robert B Gramacy and Daniel W Apley. Local Gaussian process approximation for large computer experiments. *Journal of Computational and Graphical Statistics*, 24(2):561–578, 2015.
- [16] Mengyang Gu, Kyle Anderson, and Erika McPhillips. Calibration of imperfect geophysical models by multiple satellite interferograms with measurement bias. *Technometrics*, 65(4):453–464, 2023.
- [17] Mengyang Gu and Hanmo Li. Gaussian Orthogonal Latent Factor Processes for Large Incomplete Matrices of Correlated Data. *Bayesian Analysis*, 17(4):1219 – 1244, 2022.
- [18] Mengyang Gu, Xubo Liu, Xinyi Fang, and Sui Tang. Scalable marginalization of correlated latent variables with applications to learning particle interaction kernels. *The New England Journal of Statistics in Data Science*, 1(2):172–186, 2022.
- [19] Wolfgang Hackbusch. *Iterative solution of large sparse systems of equations*, volume 95. Springer, 1994.
- [20] Mark S Handcock and Michael L Stein. A Bayesian analysis of kriging. *Technometrics*, 35(4):403–410, 1993.
- [21] Jouni Hartikainen and Simo Sarkka. Kalman filtering and smoothing solutions to temporal Gaussian process regression models. In *Machine Learning for Signal Processing (MLSP), 2010 IEEE International Workshop on*, pages 379–384. IEEE, 2010.
- [22] Trevor Hastie and Robert Tibshirani. Varying-coefficient models. *Journal of the Royal Statistical Society: Series B (Methodological)*, 55(4):757–779, 1993.
- [23] Magnus R Hestenes and Eduard Stiefel. Methods of conjugate gradients for solving linear systems. *Journal of research of the National Bureau of Standards*, 49(6):409, 1952.
- [24] Rudolph Emil Kalman. A new approach to linear filtering and prediction problems. *Journal of basic Engineering*, 82(1):35–45, 1960.
- [25] Yael Katz, Kolbjørn Tunstrøm, Christos C Ioannou, Cristián Huepe, and Iain D Couzin. Inferring the structure and dynamics of interactions in schooling fish. *Proceedings of the National Academy of Sciences*, 108(46):18720–18725, 2011.
- [26] Matthias Katzfuss and Joseph Guinness. A general framework for Vecchia approximations of Gaussian processes. *Statistical Science*, 36(1):124–141, 2021.

- [27] Matthias Katzfuss, Joseph Guinness, and Earl Lawrence. Scaled Vecchia approximation for fast computer-model emulation. *SIAM/ASA Journal on Uncertainty Quantification*, 10(2):537–554, 2022.
- [28] Genshiro Kitagawa. Monte Carlo filter and smoother for non-Gaussian nonlinear state space models. *Journal of computational and graphical statistics*, 5(1):1–25, 1996.
- [29] Clifford Lam, Qiwei Yao, and Neil Bathia. Estimation of latent factors for high-dimensional time series. *Biometrika*, 98(4):901–918, 2011.
- [30] Finn Lindgren, Håvard Rue, and Johan Lindström. An explicit link between Gaussian fields and Gaussian Markov random fields: the stochastic partial differential equation approach. *Journal of the Royal Statistical Society: Series B (Statistical Methodology)*, 73(4):423–498, 2011.
- [31] Lennart Ljung. *System identification*. Prentice Hall PTR, USA, 1999.
- [32] Fei Lu, Ming Zhong, Sui Tang, and Mauro Maggioni. Nonparametric inference of interaction laws in systems of agents from trajectory data. *Proceedings of the National Academy of Sciences*, 116(29):14424–14433, 2019.
- [33] Ryan Lukeman, Yue-Xian Li, and Leah Edelstein-Keshet. Inferring individual rules from collective behavior. *Proceedings of the National Academy of Sciences*, 107(28):12576–12580, 2010.
- [34] Yimin Luo, Mengyang Gu, Minwook Park, Xinyi Fang, Younghoon Kwon, Juan Manuel Urueña, Javier Read de Alaniz, Matthew E Helgeson, Cristina M Marchetti, and Megan T Valentine. Molecular-scale substrate anisotropy, crowding and division drive collective behaviours in cell monolayers. *Journal of the Royal Society Interface*, 20(204):20230160, 2023.
- [35] Suman Majumder, Yawen Guan, Brian J Reich, and Arvind K Saibaba. Kryging: geostatistical analysis of large-scale datasets using Krylov subspace methods. *Statistics and Computing*, 32(5):74, 2022.
- [36] Sebastien Motsch and Eitan Tadmor. Heterophilious dynamics enhances consensus. *SIAM review*, 56(4):577–621, 2014.
- [37] Giovanni Petris, Sonia Petrone, and Patrizia Campagnoli. Dynamic linear models. In *Dynamic linear models with R*. Springer, 2009.
- [38] Victor Picheny, Tobias Wagner, and David Ginsbourger. A benchmark of kriging-based infill criteria for noisy optimization. *Structural and Multidisciplinary Optimization*, 48(3):607–626, 2013.
- [39] Gianluigi Pillonetto, Francesco Dinuzzo, Tianshi Chen, Giuseppe De Nicolao, and Lennart Ljung. Kernel methods in system identification, machine learning and function estimation: A survey. *Automatica*, 50(3):657–682, 2014.
- [40] Raquel Prado and Mike West. *Time series: modeling, computation, and inference*. Chapman and Hall/CRC, 2010.
- [41] Dennis C Rapaport. *The art of molecular dynamics simulation*. Cambridge university press, 2004.

- [42] Carl Edward Rasmussen. *Gaussian processes for machine learning*. MIT Press, 2006.
- [43] Arvind K Saibaba, Alen Alexanderian, and Ilse CF Ipsen. Randomized matrix-free trace and log-determinant estimators. *Numerische Mathematik*, 137(2):353–395, 2017.
- [44] Jun Shao and Dongsheng Tu. *The jackknife and bootstrap*. Springer Science & Business Media, 2012.
- [45] Edward Snelson and Zoubin Ghahramani. Sparse Gaussian processes using pseudo-inputs. *Advances in neural information processing systems*, 18:1257, 2006.
- [46] Michael L Stein. *Interpolation of spatial data: some theory for kriging*. Springer Science & Business Media, 2012.
- [47] Michael L Stein, Jie Chen, and Mihai Anitescu. Stochastic approximation of score functions for Gaussian processes. *The Annals of Applied Statistics*, 7(2):1162–1191, 2013.
- [48] Jonathan R Stroud, Michael L Stein, Barry M Lesht, David J Schwab, and Dmitry Beletsky. An ensemble Kalman filter and smoother for satellite data assimilation. *Journal of the american statistical association*, 105(491):978–990, 2010.
- [49] Jonathan R Stroud, Michael L Stein, and Shaun Lysen. Bayesian and maximum likelihood estimation for Gaussian processes on an incomplete lattice. *Journal of computational and Graphical Statistics*, 26(1):108–120, 2017.
- [50] John Toner and Yuhai Tu. Long-range order in a two-dimensional dynamical xy model: how birds fly together. *Physical review letters*, 75(23):4326, 1995.
- [51] Aldo V Vecchia. Estimation and model identification for continuous spatial processes. *Journal of the Royal Statistical Society: Series B (Methodological)*, 50(2):297–312, 1988.
- [52] Tamás Vicsek, András Czirók, Eshel Ben-Jacob, Inon Cohen, and Ofer Shochet. Novel type of phase transition in a system of self-driven particles. *Physical review letters*, 75(6):1226, 1995.
- [53] Elise Walck-Shannon and Jeff Hardin. Cell intercalation from top to bottom. *Nature Reviews Molecular Cell Biology*, 15(1):34–48, 2014.
- [54] M. West and P. J. Harrison. *Bayesian Forecasting & Dynamic Models*. Springer Verlag, 2nd edition, 1997.
- [55] Peter Whittle. On stationary processes in the plane. *Biometrika*, pages 434–449, 1954.